EXPLOSIVE EVENTS IN THE QUIET SUN: EXTREME ULTRAVIOLET IMAGING SPECTROSCOPY INSTRUMENTATION AND OBSERVATIONS

by

Thomas Ludwell Rust

A dissertation submitted in partial fulfillment
of the requirements for the degree

of

Doctor of Philosophy

in

Physics

MONTANA STATE UNIVERSITY
Bozeman, Montana

December 2015

© Copyright

by

Thomas Ludwell Rust

2016

All Rights Reserved

APPROVAL

of a dissertation submitted by

Thomas Ludwell Rust

This dissertation has been read by each member of the dissertation committee and has been found to be satisfactory regarding content, English usage, format, citations, bibliographic style, and consistency, and is ready for submission to the Graduate School.

Dr. Charles C. Kankelborg

Approved for the Department of Physics

Dr. Yves Idzerda

Approved for The Graduate School

Dr. Carl A. Fox

STATEMENT OF PERMISSION TO USE

In presenting this dissertation in partial fulfillment of the requirements for a doctoral degree at Montana State University, I agree that the Library shall make it available to borrowers under rules of the Library. I further agree that copying of this dissertation is allowable only for scholarly purposes, consistent with "fair use" as prescribed in the U.S. Copyright Law. Requests for extensive copying or reproduction of this dissertation should be referred to ProQuest Information and Learning, 300 North Zeeb Road, Ann Arbor, Michigan 48106, to whom I have granted "the exclusive right to reproduce and distribute my dissertation in and from microform along with the non-exclusive right to reproduce and distribute my abstract in any format in whole or in part."

Thomas Ludwell Rust

December 2015

TABLE OF CONTENTS

I *MOSES-II* Optical Integration and Testing 1

1. INTRODUCTION 2

1.1 Optical Design 2
1.1.1 Changes from *MOSES-I* 5
1.2 Mirror Mounts 6
1.3 Testing Tools 7
1.3.1 Theodolite 7
1.3.2 Interferometer 8

2. *MOSES-II* OPTICAL TESTING 9

2.1 *MOSES-II* Primary Mirror 9
2.1.1 Radius of Curvature 9
2.1.2 Figure 10
2.1.3 Grating Figure Correction 11
2.2 *MOSES-II* Secondary Mirror 14
2.2.1 Wedge Angle 14
2.2.2 Figure 14

3. ALIGNMENT AND FOCUS 18

3.1 Alignment 19
3.1.1 Secondary to LOTS 19
3.1.2 Primary to Filter Tube Target 20
3.2 Focus 21
3.3 Image Quality Results 23
3.4 Grating Roll Measurement 24

4. OPTICAL MODELING 27

4.1 Fourier Optics Model 27
4.2 Results - Optical Prescriptions 29
4.3 Point Spread Functions 30
4.3.1 EUV, Modeled 30
4.3.2 Visible Light, Measured and Modeled 34
4.4 Distortion Modeling 35

TABLE OF CONTENTS – CONTINUED

II *MOSES* Observations of Explosive Events 37

5. INTRODUCTION 38

5.1 Instrument 39
5.2 Data 40
5.3 Observations 41
5.4 Discussion 48

6. NOISE MODELING 50

6.1 Introduction 50
6.2 Theory 51
6.3 Methods 54
6.3.1 Light Source 54
6.3.2 Data 54
6.4 Analysis 56
6.4.1 Read Noise and Pedestal Measurement 56
6.4.2 Signal Mean and Variance Measurement 57
6.5 Results 57
6.6 Noise at Operating Wavelength 64
6.6.1 Noise Power Spectra 67
6.6.2 EUV Noise in Wavelet Space 69

7. *MOSES-I* POINT SPREAD FUNCTIONS 73

7.1 Introduction 73
7.2 Wavelet Methods 74
7.2.1 à trous Discrete Wavelet Transform 74
7.2.2 Significance Testing 75
7.2.3 Partial Reconstruction 76
7.3 Data 77
7.4 PSF Results 80
7.5 Deconvolution 82
7.6 Temporal Variation 83
7.7 Conclusion 86
7.8 Appendix 87

8. *MOSES* INVERSIONS 90

8.1 introduction 90
8.2 Data 95
8.2.1 Synthetic Data 95
8.3 Instrument 98
8.4 Methods 99
8.4.1 à trous Discrete Wavelet Transform 99
8.4.2 Significance Testing 100
8.4.3 Partial Reconstruction from Significant Wavelet Coefficients 100
8.4.4 Deconvolution 103
8.4.5 Algebraic Reconstruction Technique 104
8.4.6 MART with Deconvolution 106
8.4.7 MART with Deconvolution and Partial Reconstruction 106
8.5 Results 107
8.6 Conclusions 112

REFERENCES CITED 114

APPENDICES 118

LIST OF TABLES

Table Page

1.1 4

2.1 Summary of test results for *MOSES-II* secondary mirror. 17

4.1 *MOSES-I* design table from Fourier optics model, using grating and secondary position and orientation from [ROGER THOMAS ZEMAX]. Grating radius of curvature is 9.48 m and grating pitch is 950 l/mm. Angles given are in degrees, and positions in mm. 29

4.2 MOSES 2 design table from Fourier optics model after moving secondary towards detectors to compensate for change in grating focal length, and adjusting the tip of the grating and secondary equally to center the detectors at z=0 . Grating radius of curvature is 9.295 m and grating pitch is 621 l/mm. Angles given are in degrees, and positions in mm. 30

1 Noise Model Parameters. See equation 6.3. 64

2 Charge Diffusion Kernel κ. Values represent the probability of a free electron being captured by a pixel in the neighborhood of the interaction site. 69

3 Wavelet space significance levels from the Atrous transform. Size scale decreases as j increases. 72

LIST OF FIGURES

Figure Page

1.1 Schematic of the *MOSES* spectrograph and coordinate system. 3

2.1 Test setup for measuring primary mirror radius of curvature. 9

2.2 Test setup for measuring primary mirror surface figure. 11

2.3 Back plate of the primary mirror mount. The three threaded shafts are the vlier screws that push the primary against the tip/tilt/focus constraints. The grid of threaded holes accepts vlier screws to apply controlled forces to the back of the mirror in an effort to correct the distorted figure. 12

2.4 Left column: Pre (top) and post (bottom) correction measured primary figure error. Right column: 120 term Zernike polynomial fits, used to obtain a smooth representation of the data. The circular indents are obscuration by the tip/tilt/focus constraint screws. The central diffracting region of the mirror is visible in the measured figure as a 5 nm deep indent relative to the surrounding surface. The white dashed circle is a circular fit to points resulting from an edge finding exercise. 13

2.5 Test setup for measuring secondary wedge angle. 14

2.6 Measured interferometer reference, stitched together from 6 partial measurements of the beam. Area is 65.3 mm × 53.0 mm. WFE is 10.7 nm RMS and 89.7 nm PV. 15

2.7 Measured *MOSES-II* figure error, composed of 7 measurements of overlapping segments of the mirror. Total area is 189.8 mm × 48.8 mm with image pixel resolution 73 μm. An imperfection in the stitching process can be seen around x = 22 mm. Tip and tilt have been subtracted. 17

3.1 Alignment tool used to reference LOTS axes. 20

3.2 Filter tube alignment target. The central square is 3.63 mm on a side which corresponds to the width of the converging (square) beam at x=211.01 mm (the target x location). The crosshairs are parallel to y and z. The circles have radii of integer multiples of 3 mm, corresponding to about 2.3' of misalignment, or a little under 10% of the field of view in the long y direction. 21

3.3 Test setup for focus. The initial wavefront defocus is precisely zeroed using a high quality flat mirror. 22

LIST OF FIGURES – CONTINUED

Figure Page

3.4 Points show measured Zernike defocus as mirror M2 is translated perpendicular to the optic axis (redirected by M1). Over-plotted red line is a linear fit.Asterisk at x=-15 shows the measured value of the Zernike defocus in the actual spectrograph. This result shows that the optical path length has to be increased by 15 mm. This focus curve is far more sensitive than, e.g., measuring visible light root mean square spot size for focus determination. 23

3.5 Air force resolution target of the aligned and focused *MOSES-II* spectrograph. Visible light, $m = 0$ spectral order. 24

3.6 Alignment of translation stage for grating roll measurement. 25

3.7 The figure shows images of a laser beam after diffraction from the grating in the $m = -1$ and $m = +1$ spectral orders. The camera was mounted to translate parallel to the y axis. The vertical difference in the spot image centroid in the two orders is practically zero, indicating good roll alignment of the primary mirror. 26

4.1 Point spread functions in *MOSES-I* three orders for varying field angle. Viewpoint is facing detectors, sun at your back, with positive z towards the top of the page. Superimposed squares represent 13.5 micron MOSES pixels. 32

4.2 Point spread functions in *MOSES-II* three orders for varying field angle using the optical design from table 4.2. Viewpoint is facing detectors, sun at your back, with positive z towards the top of the page. Superimposed squares represent 13.5 micron MOSES pixels. 33

4.3 Modeled EUV point spread functions. Top Row: point spread functions from perfect primary mirror. Center Row: point spread functions using measured primary mirror figure (§2.1.2). Bottom Row: point spread functions using corrected primary mirror figure (§2.1.3). Left to right column: $m = -1$, $m = 0$, $m = +1$. All point spread functions are normalized to total of one and displayed on the same scale. 34

4.4 Top Row from model: Full aperture, full aperture, central obscuration. Bottom Row measured: Full aperture pre flight, full aperture post flight, central obscuration post flight. Left to right column: $m = -1$, $m = 0$, $m = +1$. All point spread functions are normalized to total of one and displayed on the same scale. 35

4.5 Optical distortion in *MOSES-I* 36

4.6 example 36

5.1 *MOSES* m=0 order image taken 8 February 2006 18:47:05 UTC. Green diamonds mark the locations of the events discussed in the paper. 41

5.2 Time evolution of an explosive event observed with *MOSES*. Time increases with panel number, from 18:46:09-18:49:13 UTC. Each panel has three frames: from top to bottom, a 37.5" square subregion of I_{+1}, I_0 and I_{-1}, respectively. The frames are centered on an explosive event observed at coordinates of (433,287) in figure 5.1, about 751"S, 130"E heliocentric cartesian coordinates. Display scaling is constant. 42

5.3 Stack plots of profiles through the explosive event of Figure 1 in I_{-1} (top), I_0(center), and I_{-1} (bottom). In each panel time increases from bottom to top. Profiles were averaged over three rows passing through the center of the event to reduce noise. The component which is shifted west in I_{+1} and east in I_{-1} is blue shifted emission, and is distinctly brighter than the second component. This second component is shifted east in I_{+1} and west in I_{-1}, indicating that this emission is red shifted. The magnitude of the shifts relative to the I_0 data is three or four pixels, corresponding to doppler shifts of 90-120 km s^{-1}. 46

5.4 Examples of transient brightenings observed with *MOSES*. Each panel has three frames: from top to bottom, a 37.5" square subregion of I_{+1}, I_0 and I_{-1}, respectively. Displayed are the wavelet coefficients of the second finest scale of the DWT, calculated with the Atrous algorithm with B_3 spline scaling function. This spatial filtering helps with display. 47

6.1 Image produced with the illumination device described in §6.3.1. This image is taken with the m=-1 CCD; the other CCD illumination patterns are similar in appearance. 56

6.2 Photon transfer curve for m=-1 CCD. The data is plotted on log-log axes to show the various signal regimes. At low signal, the presence of read noise (magnitude of variance indicated by horizontal red line) results in a deviation of the transfer curve from unity slope (gray curve). At higher signal the read noise becomes insignificant compared to the Poisson distributed shot noise, and the curve takes on a characteristic slope of one, until A/D saturation is reached and the variance drops precipitously, as all pixel values approach 2^14-1 DN (vertical green line). When the read noise variance is subtracted from the total signal variance, the Poisson limited linear curve extends all the way to the zero signal level, indicating good estimation of the read noise variance. For reference the theoretical curve for pure Poisson noise is overplotted as a blue line of slope 1. 58

6.3 m=0 CCD Photon transfer curve. See figure 6.2 caption for further details. 59

6.4 m=+1 Photon transfer curve. See figure 6.2 caption for further details... 60

6.5 Histograms of estimated value of 1/G for the m=-1 CCD. The statistics are generated using NxN sub arrays of the noise images. As N is varied, the width of the histogram (which may be taken as an error estimate on the gain) varies, but the centroid remains the same. The symbols represent data, the solid lines are gaussian fits. The gain estimate results from averaging the centroids of the gaussian fits. 61

6.6 Histograms of estimated value of 1/G for the m=0 CCD. See caption of figure 6.5 for further details. 62

6.7 Histograms of estimated value of 1/G for the m=+1 CCD. See caption of figure 6.5 for further details. 63

6.8 Image produced with EUV illumination of the m=-1 CCD; the other CCD illumination patterns are similar in appearance. The contours are smoothed. The underlying grid pattern is produced by the thin metallic filter used to block visible light. 65

6.9 Noise from various sources: Synthetic (upper right), visible light measurement, m=-1 CCD (center), and EUV measurement, m=-1 CCD (lower left). All noise images are displayed on the same scale. 66

6.10 Power spectral densities of noise from synthetic (left), visible light (center), and EUV (right) data. All panels are displayed with the same scale. 68

6.11 Significance levels as function of wavelet scale for the Atrous transform applied to different noise sources. The significance levels are reduced in the EUV data, as the noise is smoothed due to charge diffusion. Note that signal to noise does not increase, as the signal is smoothed accordingly. 71

7.1 Context image. Full *MOSES* field of view. Over plotted, the red square is shown close up in figure 7.2. The green squares indicate the compact sources shown in figure 7.9. 78

7.2 Close up of the region bounded in red in figure 7.1, and its wavelet transform up to scale 4. Original images top row, m=-1,0,1 left to right. Wavelet residual (smoothed images $\mathcal{I}_s^N$) second row. Wavelet scales 4 through 1 are third through last rows. The bright object center left was the subject of a paper by [FOX ApJ]. The shape of the core is dominated by the instrument point spread function, as is the compact source just below center frame. 79

7.3 Reconstruction of a compact source for point spread function estimation, m=-1 spectral order. Each row shows an image on left, with the first and second wavelet scales to the right. Top row: original image. Middle Row: Extracted object/point spread function estimate. Bottom Row: Original image minus object. 80

7.4 Reconstruction of a compact source for point spread function estimation, m=0 spectral order. Each row shows an image on left, with the first and second wavelet scales to the right. Top row: original image. Middle Row: Extracted object/point spread function estimate. Bottom Row: Original image minus object. 81

7.5 Reconstruction of a compact source for point spread function estimation, m=+1 spectral order. Each row shows an image on left, with the first and second wavelet scales to the right. Top row: original image. Middle Row: Extracted object/point spread function estimate. Bottom Row: Original image minus object. 81

7.6 THESE DECONVOLUTION RESULTS ARE INCORRECT - NEED TO UPDATE THIS FIGURE. 83

7.7 The small active region, $\mathcal{I}_0$ data scale 1 wavelet coefficients. Each frame is at a different time, covering most of the flight with time increasing from upper left to lower right. All bright compact objects in the field of view share the same shape, which evolves over the flight. This point spread function variability may be due to thermal expansion effects. Exposures numbers are 1, 2, 4, 6, 10, 14, 18, 23 and 25, of 27 total, going in order from upper left, left to right, top to bottom. UT shown in the titles of the individual panels. 84

7.8 Same as figure 7.7, using the deconvolved data. The estimated point spread function (figure 7.4, left middle) is not ideal for early exposures. Significant resolution improvement is seen starting in the middle row (1/3 of the way through flight). It is not clear why the bottom center panel appears to suffer from increased ringing relative to the other images; otherwise, the deconvolution results towards the end of the flight are excellent. 85

7.9 Compact objects in *MOSES* data, scale 1 wavelet coefficients shown; locations shown in green in figure 7.1. Each panel has three frames, top to bottom shows m=+1, m=0, and m=-1 data. The shape of the object is very similar from panel to panel in $\mathcal{I}_0$, but sometimes shows strong variation in the dispersed orders due to doppler shifted emission. . 88

7.10 Compact objects in *MOSES* data from figure 7.9 after deconvolution. Scale 1 wavelet coefficients shown. 89

8.1 An explosive event seen by *MOSES*. Left to right: $m = -1$, $m = 0$, $m = +1$. Panels are 64×64 pixels, with angular sampling 0.59" pixel^{-1}. Dispersion in is 30 km s^{-1} pixel^{-1}. Blue shifted emission moves left (east) in $m = -1$ and right (west) in $m = +1$ relative to $m = 0$. 95

8.2 *MOSES* point spread function cores in each spectral order, estimated from the data. [RUST PSFS]. Axis units are in pixels, with angular sampling 0.59" pixel^{-1}. 96

8.3 Synthetic *MOSES* observation of a small emitting source moving with the plotted velocity profile, set on a uniformly emitting background, assuming the point spread functions of figure 8.2. Left to right: $m = -1$, $m = 0$, $m = +1$. The intensity of the source and background were chosen to approximate those in figure 8.1 (same display scale in both figures). Noise has been added to the synthetic observations consistent with *MOSES* noise model. 97

8.4 Scale 2 wavelet coefficients (top) and the significant coefficients which define the object. 102

8.5 Top: Original, Bottom: Explosive event reconstructed from the coefficients in 8.4, and Middle: Residual after reconstruction. 103

8.6 Top: Original, Middle: RL deconvolution with wavelet noise supression, and Bottom: Standard RL deconvolution 104

8.7 Projections, observed (top row) and reconstructed. Left set: real data, Right set: synthetic data. Rows, top to bottom: Observed, Method 1 (SMART), Method 2 (MART with wavelet noise suppression), Method 3(MART with deconvolution), Method 4 (MART with deconvolution and partial reconstruction)..... 110

8.8 Residuals, observed minus reconstructed. Left set: real data; Right set: synthetic data. Rows, top to bottom: Method 1 (SMART), Method 2 (MART with wavelet noise suppression), Method 3(MART with deconvolution), Method 4 (MART with deconvolution and partial reconstruction)..... 111

8.9 Slices through $\log_{10} \nu(x, y, \lambda)$. Left set: real data; Right set: synthetic data. Left column: constant y through explosive event center, x increases to right; Right column: constant x through explosive event center, y increases to right. λ axis is vertical, centered on $\lambda = 0$, increasing upwards. Rows, top to bottom: Method 1 (SMART), Method 2 (MART with wavelet noise suppression), Method 3(MART with deconvolution), Method 4 (MART with deconvolution and partial reconstruction)..... 111

8.10 Reconstructed average line profile of explosive event. Left plot: real data; Right plot: synthetic data. Method 1 (SMART), Method 2 (MART with wavelet noise suppression), Method 3(MART with deconvolution), Method 4 (MART with deconvolution and partial reconstruction)..... 112

Part I

MOSES-II Optical Integration and Testing

CHAPTER 1
INTRODUCTION

1.1 Optical Design

The *MOSES-II* spectrograph employs an off axis spherical grating (primary mirror) to form solar images in the $m = -1$, $m = 0$, and $m = +1$ spectral orders. These images are recorded on charge coupled devices (CCD) located at prime focus in each order. The optical path is split approximately in half by a flat secondary mirror. The off axis configuration is used so the secondary does not obscure the primary mirror. The *MOSES* instrument design is shown semi-schematically in figure 1.1.

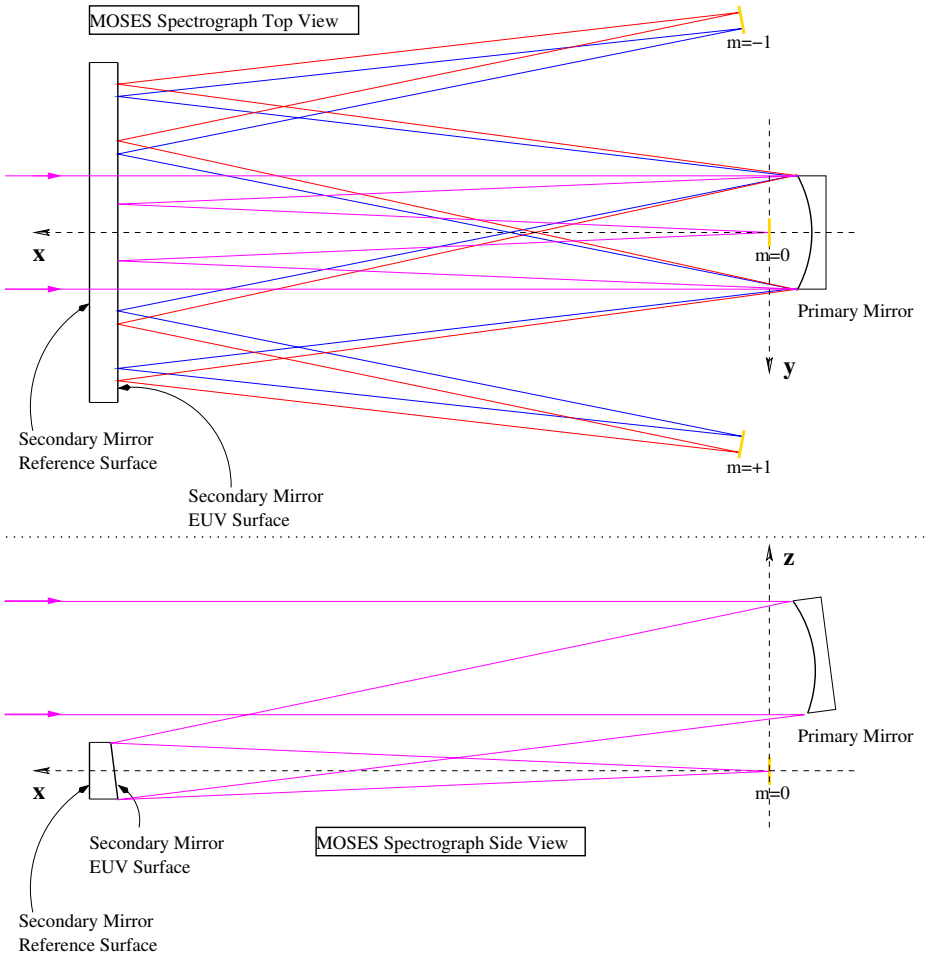


Figure 1.1: Schematic of the *MOSES* spectrograph and coordinate system.

MOSES-II optical prescription is shown in table 1.1.

Item	X	Y	Z	Pitch	Yaw
Grating	118.7	0.0	78.5	-0.993	0.0
Secondary	2382.5	0.0	0.0	+0.993	0.0
Det(+1)	3.0	-136.7	0.0	-.011	-2.463
Det(0)	0.0	0.0	0.0	-.004	0.000
Det(-1)	3.0	+136.7	0.0	-.011	+2.463

Table 1.1

MOSES-II primary mirror is a concave sphere with specified radius of curvature of 9295mm and is ruled (621 l/mm) only within a 60mm diameter circular area centered on the primary clear aperture. The profiles are optimized with intent to distribute incident light in *MOSES-II* passband equally to the $m = -1$ and $m = +1$ orders and nowhere else. The primary mirror clear aperture is an 80mm square, and balance of the aperture is not ruled, and thus puts light only in the $m = 0$ spectral order. The result is an approximately 25%, 50%, 25% distribution of intensity between the $m = -1$, $m = 0$, $m = +1$ orders respectively.

MOSES-II secondary mirror is a monolithic flat mirror with clear aperture 189.8 mm $\times$ 48.8 mm, wide enough in the dispersion direction to fold the optical path in all three spectral orders. The mirror substrate is wedge shaped when viewed from the side as in the lower panel of figure 1.1. The angled (right) facet is the multilayer coated surface. The vertical (left) hand facet of the wedge is coated for visible light reflection and is used as an alignment reference surface; therefore the wedge angle between the two surfaces must be accurately known. The specified wedge angle is 0.973 degrees.

The primary mirror surface and the EUV surface of the secondary mirror are coated with Si/Cr/Sc/Cr multilayers for 50 Åfwhm reflectance centered at 470 Å, peaking at about 0.3 [WINDT MULTILAYER: [Moses_local] Fwd: Si/Sc coating results].

1.1.1 Changes from *MOSES-I*

It was originally intended that changing *MOSES* observation wavelength would amount to changing coatings; the optical design would remain the same. Due to manufacturing limitations, however, the primary mirror design was changed significantly from the prior flight. The focal length was reduced by almost 100mm and the secondary mirror was moved closer to the primary to accommodate. A new secondary mirror mount had to be designed and fabricated for this purpose.

The specified grating pitch was not updated to reflect the change in focal length. The CCD positions in the y direction are effectively fixed. Moving the secondary towards the focal plane while keeping the diffraction angle fixed introduces an alignment offset of approximately 2.5mm, or about 10% of CCD width, between the dispersed orders and $m = 0$. This misalignment is corrected in software at a reasonable cost in reduced field of view.

Reducing the focal length calls for a change in pitch angle on the primary, or secondary, or both to maintain alignment. I chose to split the pitch change between the mirrors, reflected in the design table as in increase in grating and secondary pitch angle magnitude to 0.993 degrees from 0.973 degrees. The practical result is that there is a 0.02 degree offset in pitch between the secondary reference surface and the x axis that has to be accounted for in subsequent alignment (e.g., at the range).

1.2 Mirror Mounts

MOSES mirror mounts are mounted to a carbon fiber I-beam by way of threaded inserts embedded in the carbon fiber. The I-beam/insert structure is the Lockheed Optical Table System (LOTS). The threaded inserts are precisely located on a 4 inch grid with the mounting surfaces machined to be coplanar. Precision counterbores in the inserts accept shoulder screws for repeatable mount positioning. The I-beam and inserts thus form a precision optical bench, one capable of rocket flight. The grid axes and the normal to the mounting surfaces define *MOSES* coordinate axes. $+\hat{z}$ is normal to the insert mounting surfaces and $+\hat{x}$ points towards the sun. Angular coordinates of tip, tilt and roll are rotations about the y, z, and x axis, respectively.

MOSES alignment strategy relies on LOTS grid and precision machined mounts to position the spectrograph components within mechanical tolerance. Fine alignment and focus is completed with kinematic adjustments build into the mirror mounts. The mirrors are mounted such that each is constrained in six places, to exactly constrain the six positioning degrees of freedom: the three spatial coordinates plus tip, tilt, and roll.

The constraint is made by a hemispherical ball bearing magnetically connected to the end of a bolt which is threaded into the mirror mount. A hollow cone is machined into the bolt end to allow the spherical surface to seat; the flat surface of the hemisphere is in contact with the mirror. Magnetic connection allows the hemisphere to readily pivot on the bolt end in order to seat flush with the mirror. The mirror is pressed against each constraint with an opposing vlier screw threaded into the mount on the opposite side of the mirror.

The position of the mirror in the mount can be adjusted by changing the depth to which the the constraint bolt is threaded into the mount. The depth of these bolts are set by precision shims which sit between mount and bolt head. Three constraints contact the face of each mirror in a tripod arrangement; these constrain the telescope angular alignment and focus. I had to make new shims for these constraint screws to optimize *MOSES-II* alignment and focus (chapter 3). The remaining three constraints – two on the bottom facet and one one on the side facet of each mirror – control mirror position transverse to the optic axis, as well as the roll. I was able to reuse the *MOSES-I* shims on these constraint screws.

1.3 Testing Tools

A brief description of my two principal optical testing tools.

1.3.1 Theodolite

A theodolite is an imaging telescope with reticle eyepiece mounted for rotation in altitude and azimuth. The angular coordinates are precisely measured; angular measurements approach 1" accuracy. The theodolite is often used in autocollimation mode, with an illuminated reticle projected from the telescope, retroreflected off of a flat mirror, and received again by the telescope, forming a reverse image of the reticle. When the two reticle images are aligned the theodolite is aligned to the mirror. I used a Leica Wild T-3000 theodolite for angular alignment measurements for *MOSES-II* optical testing.

1.3.2 Interferometer

I used a PhaseCam 6000 pixellated phase mask interferometer for nanometer precision measurements of optical surface figures in a poor vibration environment (second floor, clean room fans). The measurements are proportional to optical path differences between test and reference arms of the interferometer, caused by optical surface imperfections or alignment issues. Interferometry data is often analyzed by fitting the data to sets of orthogonal polynomials. In the following I use and make reference to the Zernike polynomials.

CHAPTER 2

MOSES-II OPTICAL TESTING

This chapter describes optical testing of the *MOSES* primary and secondary mirrors.

2.1 *MOSES-II* Primary Mirror

2.1.1 Radius of Curvature

The primary mirror radius of curvature determines the spectrograph focal length. The mirror mounts have limited focus adjustment, so it is important to accurately measure the radius of curvature. Nominal radius is 9.295 m. I used a tape measure, supported along its length, to measure the distance between primary mirror surface and center of curvature. The testing setup is shown in figure 2.1.

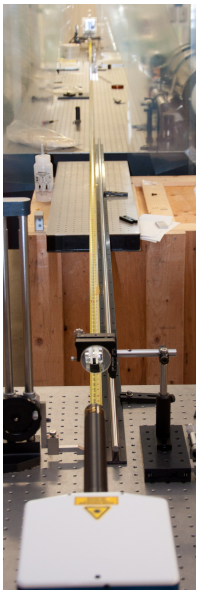


Figure 2.1: Test setup for measuring primary mirror radius of curvature.

I locate the center of curvature using an interferometer mounted with a diverging lens. The focal point of the diverging lens is coincident with the center of curvature of the primary when the Zernike defocus of the reflected wavefront is zero. I locate the diverger focal plane by translating a flat mirror along the optic axis near the focal plane until the Zernike defocus of the reflected wavefront is zeroed. The tape measure was run a few inches below the optical axis to avoid obscuration, and I use a height gage to vertically translate the "plane" of the primary mirror surface and diverger focal plane down to the tape, the difference in these measurements being the radius of curvature. The Zernike defocus between primary and interferometer suffered from noise probably due do vibration over the long measurement path. I improved the accuracy of the radius measurement by making several measurements in the neighborhood of correct radius, and fitting a line to the results. Measured radius is 9285 mm.

2.1.2 Figure

Primary mirror figure measurement was done with a PhaseCam 6000 phase shifting interferometer. In principle the measurements obtained in section 2.1.1 are measurements of the grating figure, but they are low resolution do to f/# mismatch between the interferometer diverging lens and primary mirror operated at its center of curvature (f/22 and f/120, respectively), so I used the testing arrangement shown schematically in figure 2.2.

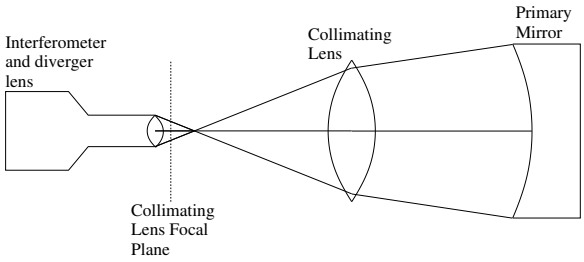


Figure 2.2: Test setup for measuring primary mirror surface figure.

The primary mirror figure measurements are corrupted by optical path length variation in the test setup. I contrived a reference measurement using the *MOSES-I* flight spare [Appendix?]. The mirror figure was out of specification, suffering from about 1.5 (46.5 nm) waves of astigmatism. The measured figure and Zernike fit is shown in the top row of 2.4.

2.1.3 Grating Figure Correction

The imaging characteristics of the primary mirror were expected to be poor, so we modified the primary mirror mount to accept vlier screws (spring loaded plungers, figure 2.3) and attempted to mechanically force the mirror to a better shape. With the primary mounted in the figure test configuration I experimented with different vlier screw positions and forces. I obtained significant reduction in the figure error using two screws. The measured primary mirror figure and Zernike fit following correction are shown in the bottom row of figure 2.4. The grating figure is analyzed in terms of expected instrument point spread functions in chapter 4.



Figure 2.3: Back plate of the primary mirror mount. The three threaded shafts are the vlier screws that push the primary against the tip/tilt/focus constraints. The grid of threaded holes accepts vlier screws to apply controlled forces to the back of the mirror in an effort to correct the distorted figure.

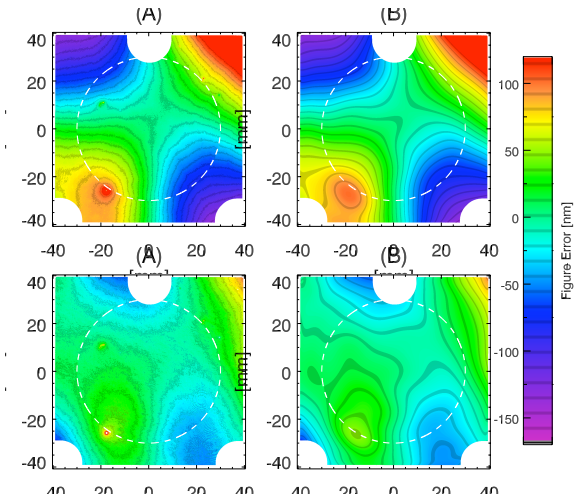


Figure 2.4: Left column: Pre (top) and post (bottom) correction measured primary figure error. Right column: 120 term Zernike polynomial fits, used to obtain a smooth representation of the data. The circular indents are obscuration by the tip/tilt/focus constraint screws. The central diffracting region of the mirror is visible in the measured figure as a 5 nm deep indent relative to the surrounding surface. The white dashed circle is a circular fit to points resulting from an edge finding exercise.

2.2 *MOSES-II* Secondary Mirror

2.2.1 Wedge Angle

I did the wedge angle measurement using a single theodolite and a precision corner cube. The testing setup is shown in figure 2.5. A theodolite in autocollimation mode is alternately aligned to the multilayer surface, then the reference surface by way of the corner cube. The wedge angle is the difference between these measurements. The secondary was mounted to permit translation into and out of the page, which I used to measure wedge angle variation at different locations along the mirror. Measured average wedge angle is 0.9738 degrees (0.973 degrees specified). 8 measurements at different locations along the y (dispersion) dimension of the mirror yields standard deviation about this value of 0.0002 degrees.

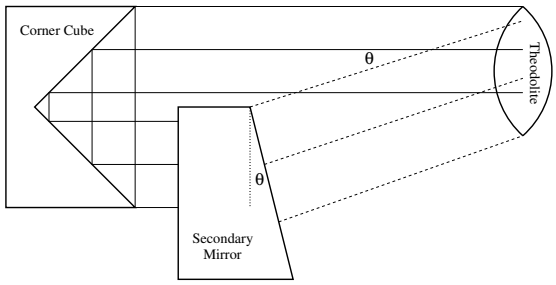


Figure 2.5: Test setup for measuring secondary wedge angle.

2.2.2 Figure

I measured the surface figure error of *MOSES-II* secondary mirror verified specification on aperture alignment, slope error and mid-scale roughness as per items 1, 2 and 3 of §4.3 of the MOSES-II Fold Flat Specification [MOSES-II FOLD FLAT SPEC]. The surface normals of the left and right sub-apertures are parallel with

that of the center sub-aperture to within a fraction of an arc second, well within the specified 5 arc seconds. Measured slope error is 1.38 μrad RMS, less than the specified 1.9 μrad RMS. Midscale roughness measures 0.71 nm RMS, less than the specification of 1.1 nm RMS.

Given the size of the secondary mirror I used a beam expander that allowed me to get the short dimension of the secondary within the interferometer field of view. The raw measurements of the secondary are dominated by systematic errors in the interferometer/beam expander system, and a reference image was required to see the true surface. I have a $\lambda/100$ flat mirror F_R of sufficient reference quality, but it's diameter is smaller than the smallest dimension of the secondary.

I made a reference image by translating F_R and making overlapping measurements of the reference surface across the interferometer field of view. I stitched the measurements together by optimizing the tip, tilt, and defocus of the reference measurements to minimize the mean absolute deviation in the overlap regions. Figure 2.6 shows the reference image measured thus, which is stitched together from 6 separate measurements.

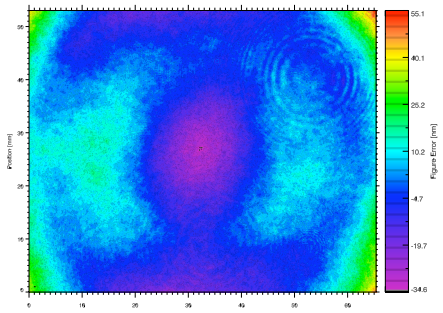


Figure 2.6: Measured interferometer reference, stitched together from 6 partial measurements of the beam. Area is 65.3 mm $\times$ 53.0 mm. WFE is 10.7 nm RMS and 89.7 nm PV.

I measured secondary in segments by translating the mirror across the interferometer beam. Each segment was reference subtracted and then stitched together like the reference image. The measured surface figure error of the secondary mirror is shown in figure 2.7

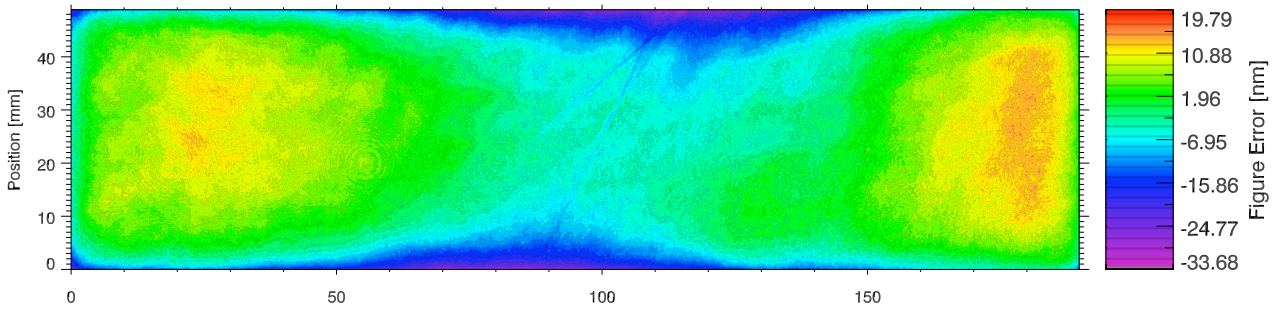


Figure 2.7: Measured *MOSES-II* figure error, composed of 7 measurements of overlapping segments of the mirror. Total area is 189.8 mm × 48.8 mm with image pixel resolution 73 μm. An imperfection in the stitching process can be seen around x = 22 mm. Tip and tilt have been subtracted.

Secondary mirror figure results are summarized in table 2.1.

MOSES-II Secondary Mirror Test Results

Spec Description	Specification	Measured
Left Aperture Alignment	$<$ 5”	.03”
Right Aperture Alignment	$<$ 5”	.07”
Slope Error	$<$ 1.9 μrad RMS	1.38 μrad
Midscale Roughness	$<$ 1.1 nm RMS	0.71 nm

Table 2.1: Summary of test results for *MOSES-II* secondary mirror.

CHAPTER 3
ALIGNMENT AND FOCUS

The critical mirror angular alignments, focus, and grating roll are described in this chapter. The optical prescription for *MOSES-II* is given in table 1.1. Alignment and focus were done without working CCDs due to failure of the *MOSES* command and data handling system, which was not repaired until after alignment was complete. The focus method described here is expected to be significantly more accurate than the method used prior. Improvement of spectrograph focus was noted as a major goal for the second flight in the *MOSES-I* final report [KANKELBORG MOSES I FINAL REPORT].

Spectrograph alignment in the dispersed orders depends on wavelength. The available alignment tools use visible wavelengths, so it's not possible to directly align the instrument in these orders. For the first flight, the system was aligned in the $m = 0$ order, and the outboard CCDs were then positioned relative to the $m = 0$ CCD according to the optical design, and the flight data show good relative focus [RUST PSF]. Reducing the primary mirror focal length does not significantly change the relative focal lengths (chapter 4), so I leave the CCDs fixed and optimize focus in $m = 0$ by changing the mirror separation.

Conceptually, alignment and focus is achieved in three steps:

1. Measure the alignment and focus state of the system from a known baseline (*MOSES-II* mirrors mounted with *MOSES-I* shims).

2. Measure the change in alignment with change in shim length.

3. Calculate new shim lengths, fabricate and install new shims, verify alignment and focus.

Alignment measurements are described in section §3.1. Focus measurement is described in §3.2.

3.1 Alignment

The coordinates in table 1.1 are referenced to LOTS axes. Two main alignment steps are required:

1. Align secondary mirror to LOTS
2. Align primary so rays parallel to $\hat{x}$ pass through the center of the $m = 0$ CCD.

3.1.1 Secondary to LOTS

MOSES spectrograph alignment is referenced to the secondary mirror alignment surface. The mount design is referenced to LOTS inserts. Therefore the secondary alignment surface has to be aligned to LOTS.

LOTS axes are measured with the tool shown in figure 3.1. Gage plugs in the insert counterbores and coplanar insert mounting surfaces keep s setup block square to LOTS axes. Gage blocks affixed to the setup block provide theodolite alignment surfaces. A theodolite aligned to the foremost gage block in figure 3.1 is looking parallel to $-\hat{x}$. Aligning a temporary reference mirror (e.g. upper left) then frees up the theodolite.

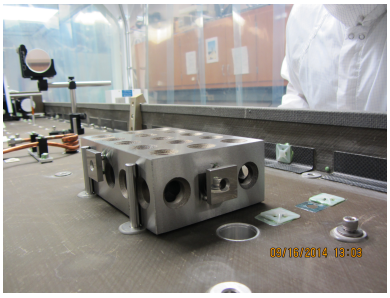


Figure 3.1: Alignment tool used to reference LOTS axes.

Once $\mathbf{x}$ is established I install the secondary mirror and measure the angular misalignment. Secondary mirror alignment is controlled by the tripod of constraint screws on the EUV surface. I had to calibrate the change in alignment to the change in shim length. I did this by using gage blocks as shims on each constraint screw in turn, measuring alignment change as I varied the gage block thickness in 0.001" increments. Now I can calculate the *relative* change in shim length required to align the secondary, but I can't calculate the absolute shim length until after I measure system focus. To proceed with alignment I temporarily align the secondary by slightly loosening one or more of the constraint screws.

3.1.2 Primary to Filter Tube Target

With the secondary aligned, the primary mirror must be aligned so that rays parallel to $\hat{x}$ are focused to the center of the $m = 0$ CCD. With the cameras inoperable I used a proxy for this alignment: a target engraved in an aluminum disc mounted to the end of the $m = 0$ order filter tube, shown in figure 3.2.

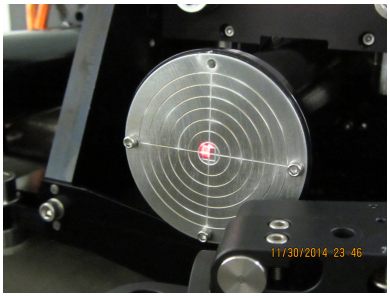


Figure 3.2: Filter tube alignment target. The central square is 3.63 mm on a side which corresponds to the width of the converging (square) beam at x=211.01 mm (the target x location). The crosshairs are parallel to y and z. The circles have radii of integer multiples of 3 mm, corresponding to about 2.3' of misalignment, or a little under 10% of the field of view in the long y direction.

I set up the theodolite so it is aligned along $-\hat{x}$ looking into the primary mirror and adjust the theodolite focus until the filter tube target is sharp. Angular misalignment of the primary is the angular difference relative to the target center, measured with the theodolite. As with the secondary mirror, the primary mirror pointing is controlled by the tripod of constraint screws on the EUV surface, and again I had to calibrate the change in shim length to the change in angular alignment. I did this in a similar fashion to the secondary angular alignment calibration, this time using 0.001" shim washers, as the 0.5" constraint screws do not accept gage blocks. This completes the required angular alignment measurements.

3.2 Focus

The shims which control angular alignment also determine the **x** location of the mirrors and thus spectrograph focus. Therefore system focus state must be known before the shim lengths can be adjusted properly.

Proper focus results in the smallest size spot on the CCD. Traditional focus methods rely on through focus spot size measurements where the optical path is changed and the resulting spot size is measured. The cameras were not operable so I came up with a different focus method shown in figure 3.3.

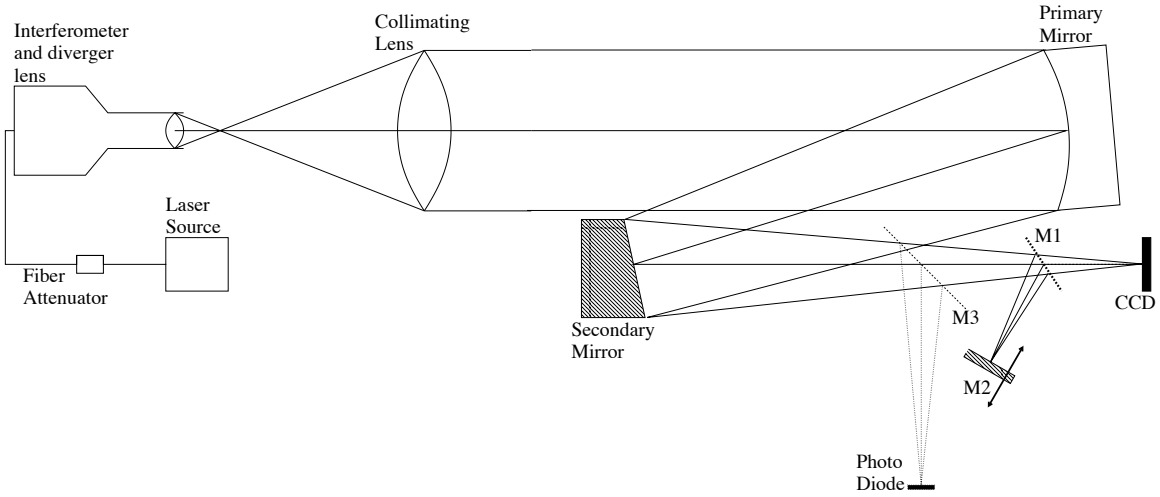


Figure 3.3: Test setup for focus. The initial wavefront defocus is precisely zeroed using a high quality flat mirror.

I use an interferometer to measure the curvature in an initially flat wavefront passed though the spectrograph and retro reflected by the CCD back to the interferometer. The Zernike defocus of the reflected wavefront is directly proportional to required change in shim length to achieve best focus. I calibrated the measurements by redirecting (with flat mirror M1) the converging beam to a flat mirror (M2) which is used to measure the wavefront Zernike defocus as M2 is precisely translated through the focus of the converging beam. This serves the same function as translating the CCD but is significantly easier and carries less risk for the sensitive camera system. The location of the measured spectrograph defocus on the calibration curve determines the required change in shim length to achieve focus. Figure 3.4 shows the

results of the focus measurement, using the *MOSES-I* shims as a baseline to focus the *MOSES-II* optics.

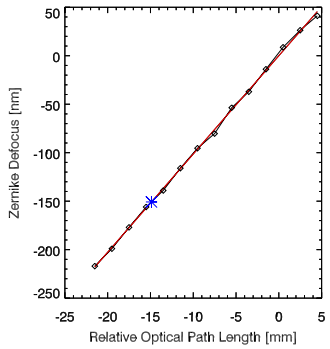


Figure 3.4: Points show measured Zernike defocus as mirror M2 is translated perpendicular to the optic axis (redirected by M1). Over-plotted red line is a linear fit.Asterisk at x=-15 shows the measured value of the Zernike defocus in the actual spectrograph. This result shows that the optical path length has to be increased by 15 mm. This focus curve is far more sensitive than, e.g., measuring visible light root mean square spot size for focus determination.

3.3 Image Quality Results

Alignment and focus were completed prior to repairs to *MOSES* flight computer, hence the cameras were inoperable. The first true images taken with the *MOSES-II* spectrograph were taken using the big collimator at White Sands Missile Range during our launch campaign. A sample image of a resolution test target is shown in figure 3.5. Pre and post flight visible light point spread functions were also measured at MSU, these are shown in the following chapter.

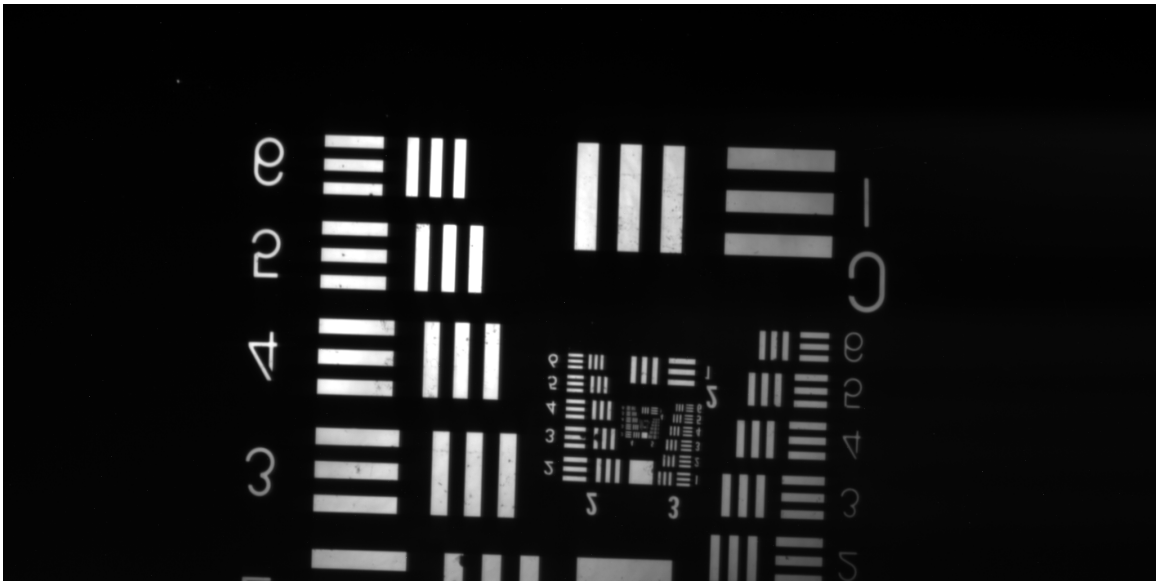


Figure 3.5: Air force resolution target of the aligned and focused *MOSES-II* spectrograph. Visible light, $m = 0$ spectral order.

3.4 Grating Roll Measurement

I verified that the grating roll angle put the dispersion in the $x - y$ plane by direct measurement. With a laser beam aligned to the optic axis, I used the LOTS alignment tool to align a stage (figure 3.6) to translate a CMOS camera parallel to the y axis and precisely measured the height (z) of the diffracted beam in the $m = -1$ and $m = +1$ orders. The results (figure 3.7) show the dispersion plane is effectively parallel to the $x - y$ plane, as intended.

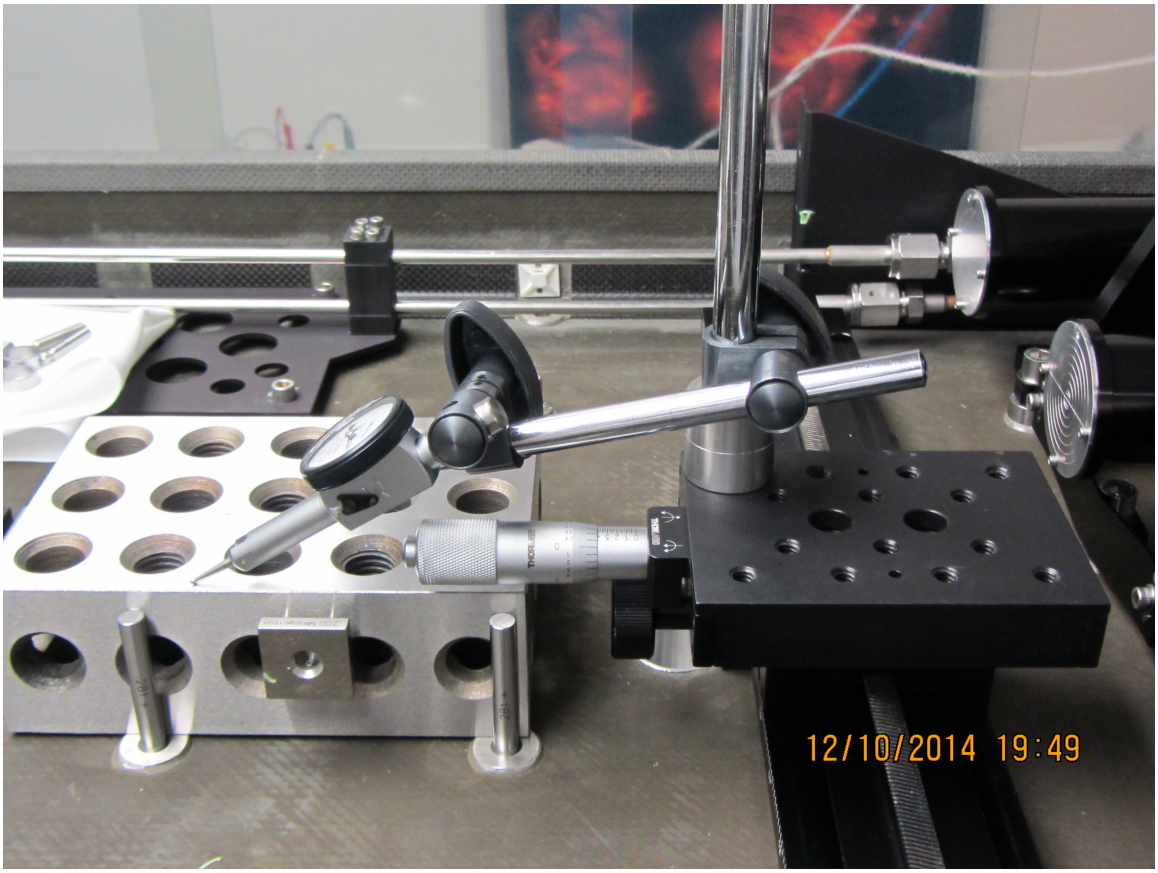


Figure 3.6: Alignment of translation stage for grating roll measurement.

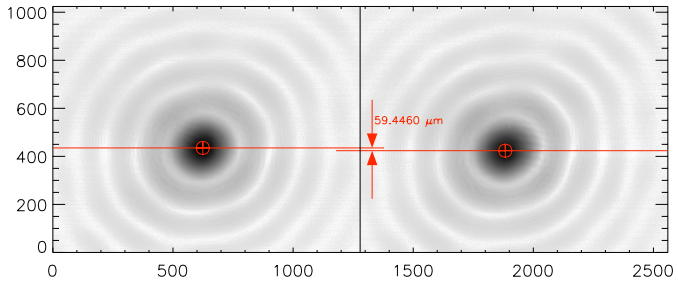


Figure 3.7: The figure shows images of a laser beam after diffraction from the grating in the $m = -1$ and $m = +1$ spectral orders. The camera was mounted to translate parallel to the y axis. The vertical difference in the spot image centroid in the two orders is practically zero, indicating good roll alignment of the primary mirror.

CHAPTER 4
OPTICAL MODELING

In this chapter I use a use a Fourier optics model to estimate optical performance of the *MOSES* spectrograph.

4.1 Fourier Optics Model

The electric field distribution near *MOSES* ideal focal plane due to a distant source of illumination is modeled as

$$E(\vec{f}+\vec{\delta}) = \iint E_0(y',z') e^{ik\left(|\vec{f}-\vec{r}|-\frac{m\lambda y'}{d}\right)} e^{-i2\pi\left(\frac{\delta_y}{\lambda f}y'+\frac{\delta_z}{\lambda f}z'\right)} dy'dz' \tag{4.1}$$

Here, $\vec{f}=(y,z,x)$ is the nominal focal point, $\vec{\delta}=(\delta_y,\delta_z,\delta_x)$ is a small displacement perpendicular to $\vec{f}$, $\vec{r}=(y',z',x'(y',z'))$ is the position vector on the surface of the grating, m is the diffraction order, and d is the grating pitch. The grating rulings are modeled a phase contribution which is linear along the dispersion direction. $E_0(y',z')$ is the incident electric field evaluated on the mirror surface, which for a unit amplitude plane wave is given by

$$E_0 = e^{i\vec{k}\cdot\vec{r}} \tag{4.2}$$

where $\vec{k}$ is the incident wave vector.

The integral on the right of 4.1 is a function of spatial frequencies $(v,w)=\left(\frac{\delta_y}{\lambda f},\frac{\delta_z}{\lambda f}\right)$ whose sampling interval and range are given by the usual sampling considerations, i.e.,

$$\delta v = \frac{1}{\Delta y'} \quad , \quad \Delta v = \frac{1}{\delta y'} \tag{4.3}$$

Given $\delta y', \Delta y', \delta z', \Delta z'$ as the sampling interval and range in the aperture plane the sampling interval and range in the focal plane are therefore given by

$$\delta\delta_y = \frac{\lambda f}{\Delta y'} \quad , \quad \Delta\delta_y = \frac{\lambda f}{\delta y'} \tag{4.4}$$

$$\delta\delta_z = \frac{\lambda f}{\Delta z'} \quad , \quad \Delta\delta_z = \frac{\lambda f}{\delta z'} \tag{4.5}$$

δ_x is given by the condition that $\vec{\delta} \cdot \vec{f} = 0$.

The diffraction code consists of the following steps:

- Define grating parameters, and grating and secondary positions and orientations.
- Define incident light wavevector based on input incidence angles (altitude and azimuth).
- Define grid of grating coordinates based on input desired number of points and maximum range of aperture coordinates.
- Estimate nominal focus position $\vec{f}$.
- Use optimization procedure to minimize the phase term under the integral in the diffraction formula as a function of $\vec{f}$, using the guess from the previous step as a starting point.
- Repeat steps 2-5 for several incident light directions spanning a 20' (azimuth) by 10' (altitude) field of view, and for each of the three spectral orders m = -1,0,1.
- Fold the calculated $\vec{f}$ vectors via the secondary mirror.

- Subtract off the vector $\vec{f_0}$, the (folded) position vector of the best focus for on axis illumination in the zero order. This step shifts the coordinate system origin to the center of the m=0 order detector.

- For each of the three spectral orders, fit a plane to the best focus positions. These planes give the detector positions and orientations.

4.2 Results - Optical Prescriptions

I tested the code by first modeling the *MOSES-I* spectrograph and comparing the results (Table 4.1) with the original ZEMAX model [ROGER THOMAS ZEMAX]. The Fourier model results are almost identical.

MOSES 1 Design Table from Fourier Optics Model

Item	X	Y	Z	Pitch	Yaw
Grating	118.8	0.0	78.5	-0.973	0.0
Secondary	2428.7	0.0	0.0	+0.973	0.0
Det(+1)	3.0	-136.9	0.0	-.003	-2.480
Det(0)	0.0	0.0	0.0	-.001	0.000
Det(-1)	3.0	+136.9	0.0	-.003	+2.478

Table 4.1: *MOSES-I* design table from Fourier optics model, using grating and secondary position and orientation from [ROGER THOMAS ZEMAX]. Grating radius of curvature is 9.48 m and grating pitch is 950 l/mm. Angles given are in degrees, and positions in mm.

I modeled *MOSES-II* with the secondary moved towards the detectors to accommodate the reduced focal length of the grating, and the grating and secondary tips

optimized to center the detectors at z=0. Table 4.2 shows the resulting optical design table. The outboard detectors are required to move in (towards $m = 0$) by about 2.7 mm or a loss of 10% of the usable field of view will result. The tip of the secondary should not present any extra difficulty in the optical alignment.

MOSES-II Design Table

Item	X	Y	Z	Pitch	Yaw
Grating	118.8	0.0	78.5	-0.993	0.0
Secondary	2382.5	0.0	0.0	+0.993	0.0
Det(+1)	2.9	-134.2	0.0	.005	-2.478
Det(0)	0.0	0.0	0.0	-.001	0.000
Det(-1)	2.9	+134.2	0.0	.000	+2.477

Table 4.2: MOSES 2 design table from Fourier optics model after moving secondary towards detectors to compensate for change in grating focal length, and adjusting the tip of the grating and secondary equally to center the detectors at z=0 . Grating radius of curvature is 9.295 m and grating pitch is 621 l/mm. Angles given are in degrees, and positions in mm.

4.3 Point Spread Functions

4.3.1 EUV, Modeled

I used the model to estimate point spread functions at operating wavelength across the field of view in each spectral order. I've shown the model results from *MOSES-I* (figure 4.1) and *MOSES-II* (figure 4.2) to show how the change the grating changes the expected instrument point spread functions. Limiting the aperture in the dispersed

orders tightens up the point spread functions; conversely, the central order point spread function is expected to get a little worse as the aperture in that order is limited.

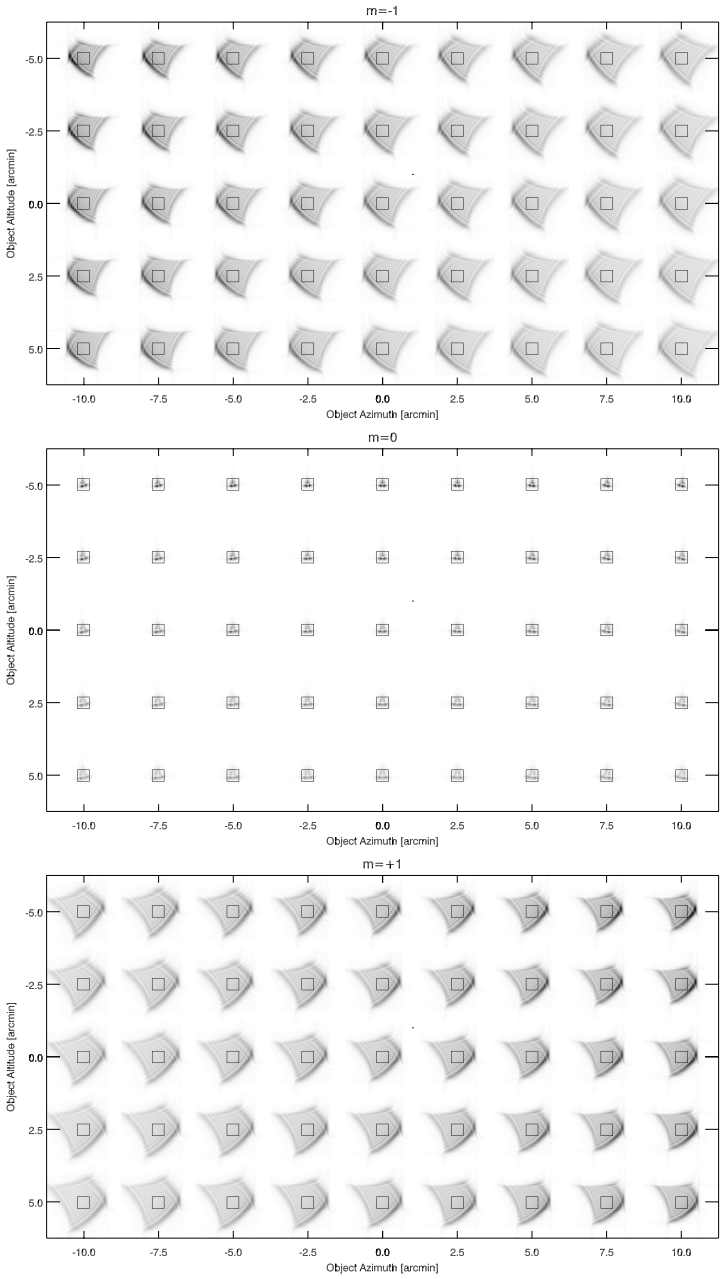


Figure 4.1: Point spread functions in *MOSES-I* three orders for varying field angle. Viewpoint is facing detectors, sun at your back, with positive z towards the top of the page. Superimposed squares represent 13.5 micron MOSES pixels.

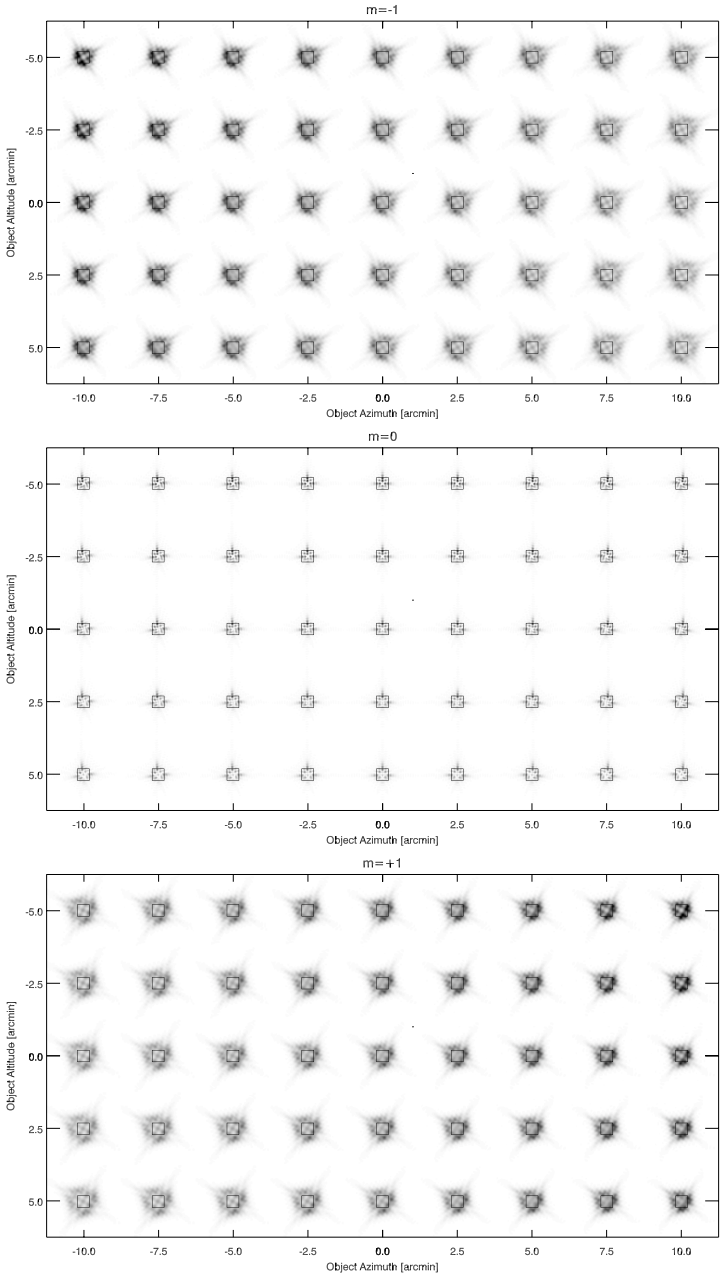


Figure 4.2: Point spread functions in *MOSES-II* three orders for varying field angle using the optical design from table 4.2. Viewpoint is facing detectors, sun at your back, with positive z towards the top of the page. Superimposed squares represent 13.5 micron MOSES pixels.

I incorporated the measured figure error of the primary mirror (shown in figure 2.4) into the model as added path difference, and estimated point spread functions pre and post correction. These results are shown in figure 4.3 with spatial sampling of 13.5 μm (*MOSES* CCD sampling).

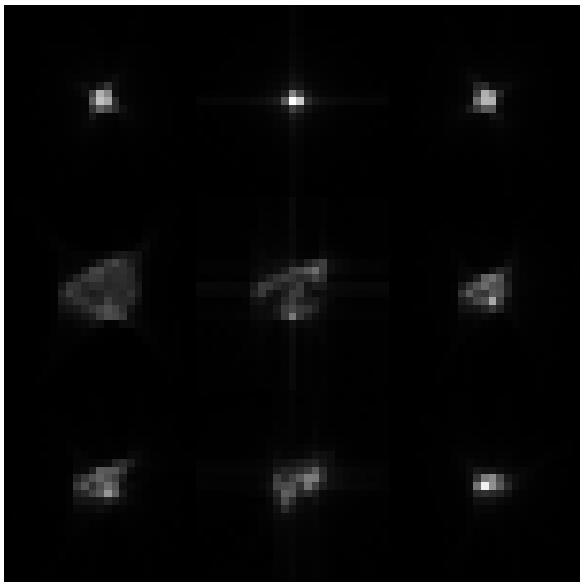


Figure 4.3: Modeled EUV point spread functions. Top Row: point spread functions from perfect primary mirror. Center Row: point spread functions using measured primary mirror figure (§2.1.2). Bottom Row: point spread functions using corrected primary mirror figure (§2.1.3). Left to right column: $m = -1$, $m = 0$, $m = +1$. All point spread functions are normalized to total of one and displayed on the same scale.

The correction shows great promise for improving *MOSES-II* image quality.

4.3.2 Visible Light, Measured and Modeled

Subsequent to alignment, and prior to going to the range, undergraduate student Roy Smart and I measured the $m = 0$ point spread function in visible ($\lambda = 635nm$)

light. An interferometer and beam expander arrangement was used, so precise collimation was achieved by adjusting the system until the measured Zernike defocus of a high quality flat mirror interposed into the beam was zero. We repeated the measurement post flight, and also thought to obscure the central diffracting region of the primary mirror, so the $m = 0$ aperture was approximately as it is at operational wavelength. The results are shown in figure 4.4.

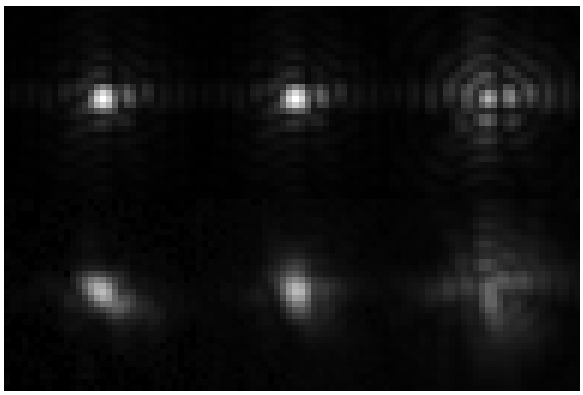


Figure 4.4: Top Row from model: Full aperture, full aperture, central obscuration. Bottom Row measured: Full aperture pre flight, full aperture post flight, central obscuration post flight. Left to right column: $m = -1$, $m = 0$, $m = +1$. All point spread functions are normalized to total of one and displayed on the same scale.

4.4 Distortion Modeling

Optical distortion could be an issue with the MOSES spectrograph which is sensitive to alignment between spectral orders. I modeled the optical distortion in *MOSES-I* by comparing focus spot centroids in the detector planes as a function of field angle – $m = -1$ relative to $m = 0$ (figure 4.5), and $m = +1$ relative to $m = 0$ (figure 4.5). The model shows a ramp in distortion which reaches a magnitude of approximately

1 pixel towards the corners of the field of view. The *MOSES* digital co-alignment routine employs a linear warping of the images to minimize the impact of distortion. This type of model could be useful to constrain the co-alignment.

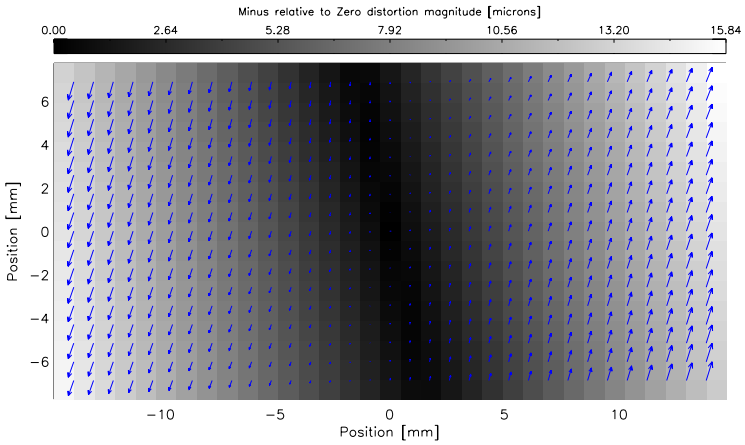


Figure 4.5: Optical distortion in *MOSES-I*

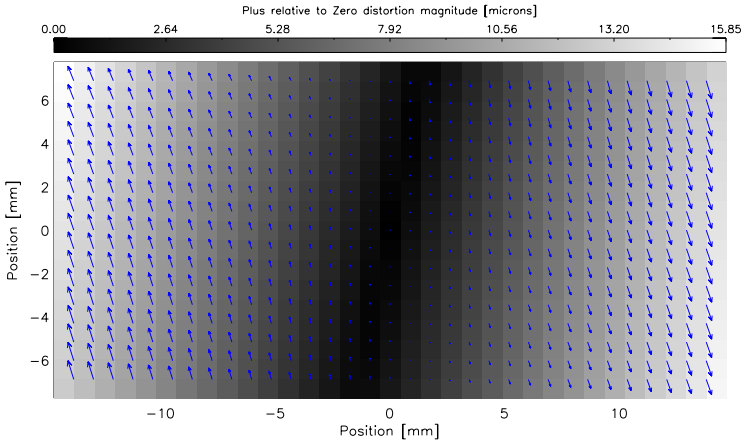


Figure 4.6: example

Part II

MOSES Observations of Explosive Events

CHAPTER 5
INTRODUCTION

Many observations have been made of small energetic events in the solar transition region. Broad interest in the topic is assured by the potential that these events are observational signatures of processes which may contribute significant energy and mass into heating and populating the corona ([1]). Transient phenomena have been observed in both image and spectrograph data, and nomenclature tends to be based on appearance in the data of choice. Broadly, the term bright point has been used to describe observations of compact stochastic brightening in image data. Explosive event generally describes compact brightening with broad non gaussian wings observed in slit spectra of transition region spectral lines [2]. Both phenomena have been linked to photospheric magnetic flux cancellation([3], [4]). Explosive events have been interpreted as the spectral signature of reconnection outflows ([3], [5]). Alternatively it has been suggested that they are the signature of helical motion ([6]). Understanding these phenomena requires combined image and spectral information. Combined image and spectral studies have been done with rastering ([5]) and multiple instrument observations ([7], [8], [9]). IRIS uses a slit jaw imager to provide context for spectral data, but rastering or sit and stare are still required for imaging spectroscopy ([10]). The Multi-Order Solar EUV Spectrograph (*MOSES*) is designed for snapshot EUV imaging spectroscopy. An explosive event observed with *MOSES* captured rapid dynamics which could not have been recorded with rastering ([11]). I've used *MOSES* to survey bright points and explosive events in He II 304 ÅI'll show 45 compact transient events observed with *MOSES*, most chosen to exhibit explosive event characteristics. Using *MOSES* unique capabilities it is possible to get spectra

from all bright points in the field of view, simultaneously, which is not possible with slit spectroscopy.

5.1 Instrument

MOSES is a slitless imaging spectrometer ([12]). The instrument forms solar images in 3 spectral orders – $m = 0$, $m = -1$ and $m = +1$ – of a concave diffraction grating. A multilayer coating restricts the passband to a narrow region centered on the He II 304 Å spectral line. The images are recorded simultaneously with three 2048×1024 pixel CCD cameras (0.59"/pixel). Each exposure in the *MOSES* data set contains three images: I_{-1}, I_0, and I_{+1}. I_0 is a narrowband multilayer He II 304 Å image. I_{-1} and I_1 are dispersed images and contain a mixture of spatial and spectral information: the measured coordinates of an emitting source depends on both the location and the wavelength of the emission. Following suitable coalignment, a source emitting at HeII line center will image to the same location on each detector. Spectral information is obtained by comparison of the intensity distribution amongst the images. The equation for *MOSES* image formation of object $v(x', y', \lambda)$ in order m is ([12])

$$I_m(x', y') = \int_B v(x' - m\lambda, y', \lambda) d\lambda \tag{5.1}$$

where (x', y') are detector coordinates and B is the instrument passband. In practice this equation needs to be modified by convolution with the order dependent point spread function $\mathcal{P}_m$. In the special case of an unresolved (e.g., small compared to the size of $\mathcal{P}_m$), isolated object v, equation 5.1 reduces to the result expected from a slit spectrograph, i.e., the line profile of the object convolved with the instrument point

spread function. This property along with high cadence and wide field of view make *MOSES* an excellent instrument for studying explosive events.

5.2 Data

Observations were made during the first flight of *MOSES* on 2006 February 8, with 27 exposures obtained from 18:44:17-18:49:13 UTC ([11]). Exposure time varies between 0.25 s to 24 s with approximately 4 s readout time. A sequence of 15 3 s exposures were made mid flight, yielding approximately 1:45 of observation with uniform 7 s cadence. The raw images were dark subtracted and corrected for flat field. The images are co-aligned using a linear polynomial distortion, and normalized to have equal intensity integrated over all non saturated image pixels. See [11] for more details.

Solar coordinates are obtained from co-alignment of I_0 with a co-temporal *SOHO-EIT* 304 Å image via cross correlation. *MOSES* images are oriented with solar north up and solar west to the right. The instrument field of view is approximately [1004"E, 197"W] by [302"S,299"N] heliocentric cartesian coordinates. The dispersion direction is E-W. Sources emitting to the blue of He II 304 Å line center move west in I_{+1} and east in I_{-1}; sources to the red are shifted in the opposite sense. The dispersion is 30 mÅ pixel^{-}1, corresponding to a doppler shift of 30 km s^{-}1 pixel^{-}1.

The events were chosen subjectively. Candidate locations were chosen based on significant disparity between I_0 and the dispersed orders, indicating doppler shifted emission, in conjunction with small scale brightening, where emission power versus scale is based on the discrete wavelet transform. The displayed events were chosen based on what appeared in interesting upon viewing movies of the events. These

events are not meant to represent a statistical survey or exhaustive catalogue of small scale energetic phenomena observed with *MOSES*, merely a collection of interesting examples.

Figure 5.1 shows an I_0 image from the 2006 flight, overlaid with the locations of the objects presented in this letter.

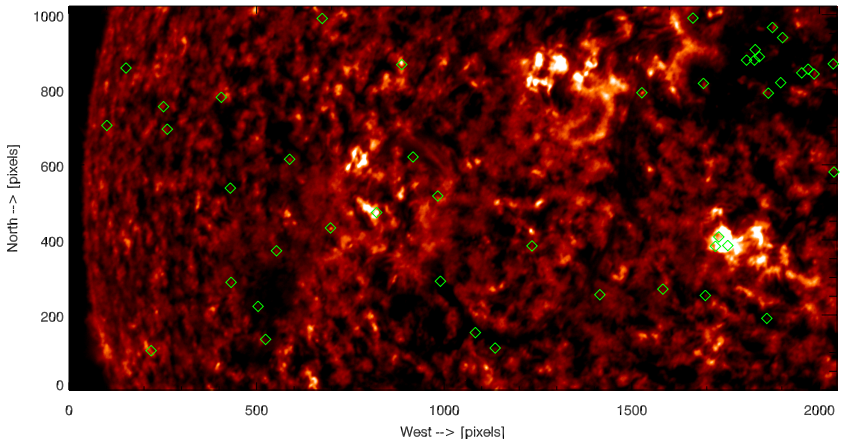


Figure 5.1: *MOSES* m=0 order image taken 8 February 2006 18:47:05 UTC. Green diamonds mark the locations of the events discussed in the paper.

5.3 Observations

Figure 5.2 shows an explosive event observed with *MOSES*. The wavelength integrated intensity of the event is seen in the middle frame of each panel (I_0). The event appears as a compact (4") patch which brightens through panel 9, then fades somewhat. It is visible until panel 17, giving a minimum event lifetime of 160 s, but may extend beyond our observation period. The shape and size of the brightening remains essentially constant over the observation period; no sky plane motion is apparent.

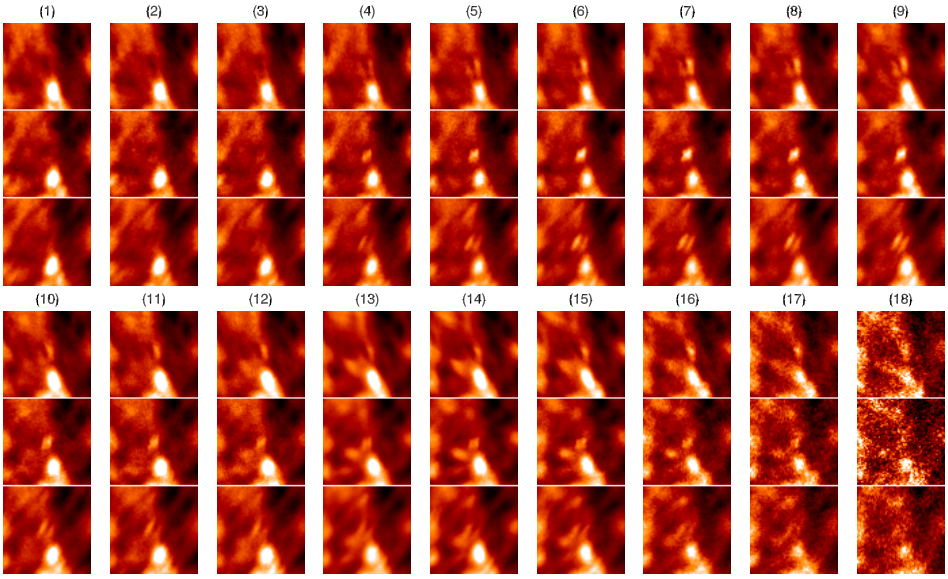


Figure 5.2: Time evolution of an explosive event observed with *MOSES*. Time increases with panel number, from 18:46:09-18:49:13 UTC. Each panel has three frames: from top to bottom, a 37.5" square subregion of I_{+1}, I_0 and I_{-1}, respectively. The frames are centered on an explosive event observed at coordinates of (433,287) in figure 5.1, about 751"S, 130"E heliocentric cartesian coordinates. Display scaling is constant.

Spectral information is obtained from the dispersed images I_{+1} and I_{-1} (top and bottom frames). The brightening in each of these images shows two distinct components, one shifted to the east, and one to the west, relative to the brightening in I_0. A distinct gap is seen between the components. The shifts indicate that the emission is doppler shifted, with one blue shifted and one red shifted component. The gap indicates significantly less emission from low velocity plasma relative to the shifted emission. The distinct shapes of the components - east leaning slashes in I_{+1}, west leaning slashes in I_{-1}, and the rectangular shape of the event in I_0 - are due to the instrument point spread functions, different in each order.

The question of emission or lack thereof from near line center is of great interest. Despite the point spread functions, the clearly dominant spectral characteristics of the explosive event in this example are fast doppler shifted components, which might be interpreted as oppositely directed flows. The gap between the shifted components seen in I_{+1} and I_{-1} indicate a paucity of emission near line center. Emission from plasma at low velocity, if it exists, is much fainter than that from high speed plasma.

Although the event is spatially unresolved, evidence of structure is seen as a vertical offset that develops between the shifted components. Most clearly seen in panel 9, the brighter, blue shifted component appears to be a few pixels north of the dimmer red shifted component. This offset of blue and redshifted components has often been reported in slit spectrograph observations of explosive events. The offset appears to evolve in time, e.g., the components appear side by side prior to about panel 7, and appear clearly offset in panels 9-11. In later frames it may be that the offset again diminishes, although diminishing signal to noise as the event fades makes this determination difficult.

Figure 3 shows stack plots of the E-W (dispersion direction) profiles through the center of the explosive event for each panel of figure 5.2. The brightest row corresponds to panel 9 in figure 5.2. The m=0 stack plot tracks changes in the event light curve; E-W shifts of 3-4 pixels in the dispersed orders indicates 90-120 km s^{-}1 oppositely directed line of sight plasma motions.

The event brightens until panel 9, then fades, with perhaps another increase in brightness towards the end of the observation. No acceleration period is observed at the onset of the event; the shifts are present and approximately 100 km s^{-1} when first detectable. The doppler magnitudes of the shifted components are relatively stable over the observation period, with perhaps some acceleration of the blue component over the end half of the observation period.

A selection of transient brightenings observed with *MOSES* with coordinates indicated in figure 5.1 are shown in figure 5.4. Each panel is a snapshot of a bright point. The panels are arranged as in figure 5.2. Observation time varies from panel to panel, but generally increases from upper left to lower right. The images have been filtered to isolate small features. The general shapes of the instrument point spread functions are seen in the similar morphology among events observed in a given spectral order.

The observation from panel 9 in figure 5.2 is shown in panel (29) of figure 5.4. The characteristic splitting of the emission in the dispersed orders, indicating fast, oppositely directed flows with little to no line center emission, is clearly seen in other examples (e.g., (1-4,11,14,17,24)). (3-4) are bidirectional with strong blue dominance. (7) is an extended object, and may be two adjacent events, each having spectra consistent with supersonic bidirectional flow. (20), another extended object, shows a clear change from red shift dominance to blue shift dominance as position moves north along the event. Some events have clear splitting in one dispersed order, while the other order is less distinct, e.g., (5,9,19,26), I_{+1} split, and (7,11,21,27), I_{-1} split. (12) lies at the western edge of the field of view, so the m=+1 data are missing, but the $m = -1$ order shows an extremely distinct splitting. Some events appear to have only a single supersonic component, e.g., (31,33,40), blue shift only, (10), red shift only. Events (22,36) may be broadened spectra, or they might be two component spectra with speeds at or below *MOSES* spectral resolution. (23) and (32) are complicated, dynamic events. The bright core in (23) shows strong blue shift, with complicated doppler activity and brightness changes leading up to this frame. The fainter object almost directly left of the core has just been expelled from the region of the core and shows both sky plane and line of sight motion. The event in panel (32) is the same as that reported in ([11]), a few exposures prior to the exposure used in that study. This event is unusually bright, has the strongest doppler shifts observed thus far in the

MOSES data set (150 km s−1), and shows complicated sky plane motions. Panels (42-45) illustrate the instrument point spread functions. Compact brightenings with unresolved spectra take on the shape of the point spread functions.

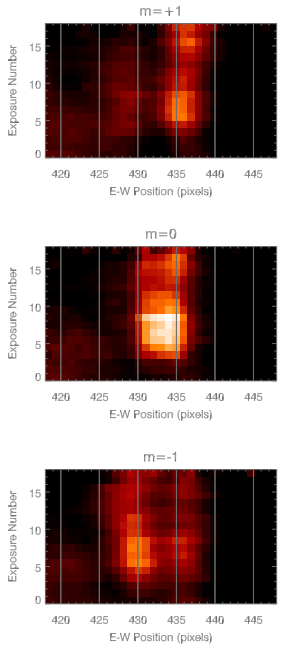


Figure 5.3: Stack plots of profiles through the explosive event of Figure 1 in I_{-1} (top), I_0(center), and I_{-1} (bottom). In each panel time increases from bottom to top. Profiles were averaged over three rows passing through the center of the event to reduce noise. The component which is shifted west in I_{+1} and east in I_{-1} is blue shifted emission, and is distinctly brighter than the second component. This second component is shifted east in I_{+1} and west in I_{-1}, indicating that this emission is red shifted. The magnitude of the shifts relative to the I_0 data is three or four pixels, corresponding to doppler shifts of 90-120 km s^{-1}.

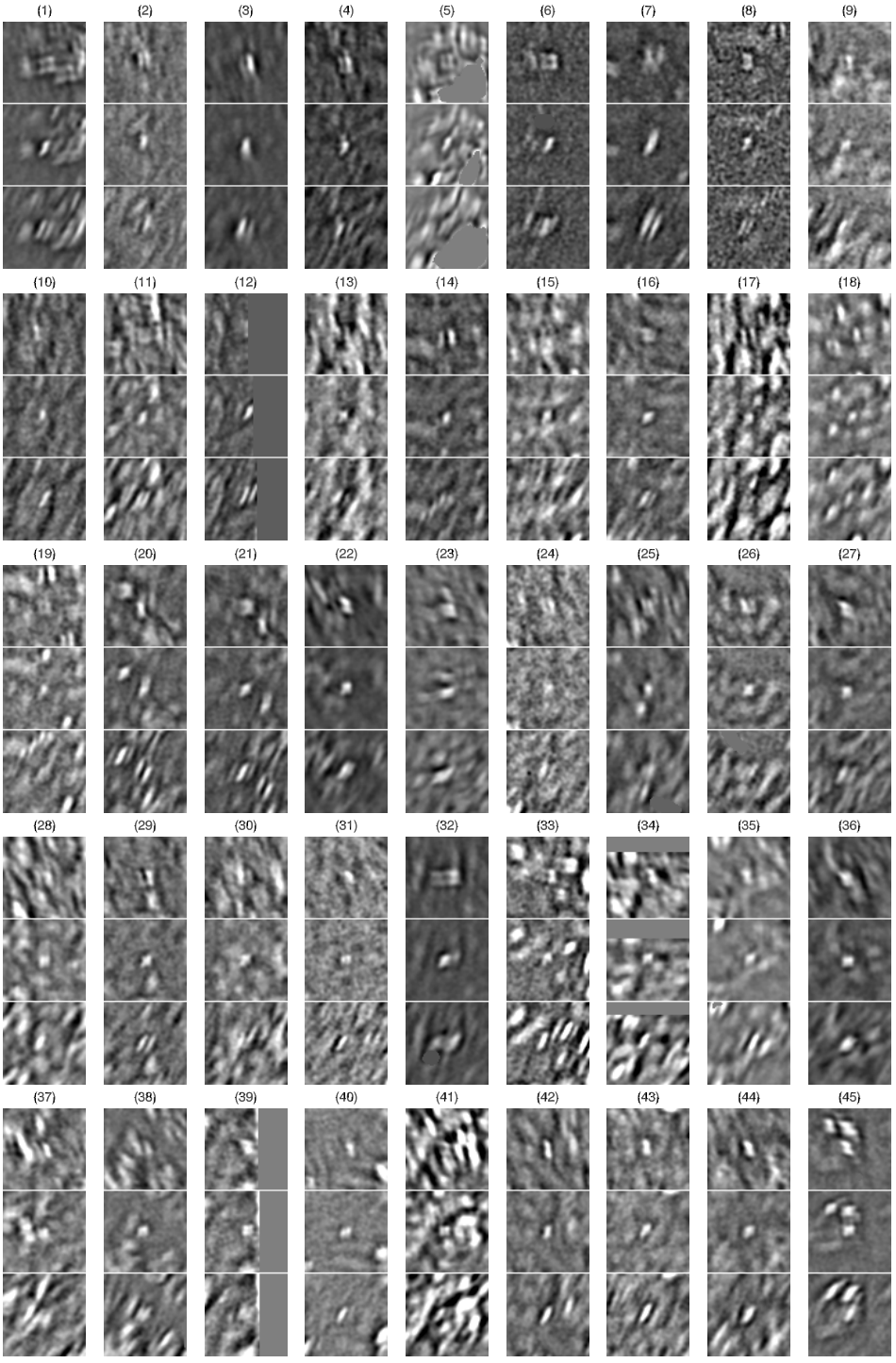


Figure 5.4: Examples of transient brightenings observed with *MOSES*. Each panel has three frames: from top to bottom, a 37.5" square subregion of I_{+1}, I_0 and I_{-1}, respectively. Displayed are the wavelet coefficients of the second finest scale of the DWT, calculated with the Atrous algorithm with B_3 spline scaling function. This spatial filtering helps with display.

5.4 Discussion

Variability exists in the examples presented, but we clearly see examples in *MOSES* data that could be described as jets (single fast component, blue or red), and explosive events. The explosive event examples, with the event from figure 5.2 as the archetype, are interesting because they clearly show fast shifted components, with little emission at line center. Background emission surely has a line center component, but it is not ambiguous that emission at line center for these explosive events, if present, is very weak relative to the doppler shifted emission. These spectra are evocative of Petscheck reconnection outflows along the line of sight.

This may be contrasted with frequent observations which describe enhancement of the line center emission in explosive events (e.g., [13]). These are very different explosive event spectra than what we observe. One possibility is that these events are fundamentally different phenomena. Another possibility is suggested by figure 17 in ([13]). In this paper the authors attribute SiIV line core enhancement observed in explosive events with IRIS to low velocity plasma trapped in magnetic islands formed between nearby reconnection sites. Model spectra show that early in the reconnection process the event spectra should look like what we observe with *MOSES*, with core brightening occurring some minutes later. We may be observing an explosive event at an earlier stage of development, prior to the core formation. A third conjecture is that we are observing an early stage of reconnection outflows, when the flow is laminar. Perhaps the outflow jets become turbulent prior to heating to the point that emission becomes visible in hotter lines.

It has been suggested that the spectral signatures of explosive events are better explained with helical motion, as with rotating spicules. Our explosive event observa-

tions may be consistent with observation of a rotating body viewed near perpendicular to its rotation axis, although our velocities are higher by a factor of three than the example in [6]. With careful analysis it may be possible to make a statistical judgement of the level of emission at line center. This must be present if the rotational model is correct, and should not be there for the Petschek model, providing a way to choose between interpretations.

Some of the events in the *MOSES* data show rapid sky plane motion, with dynamics that cannot be captured by rastering with any existing slit spectrograph. Other events, as with the explosive event in figure 5.2, show little discernible motion. Observed explosive events from limb to disk center show similar doppler shift magnitudes and no sky plane motion. This is difficult to explain in the context of oppositely directed doppler flows along a defined axis. It is also noted that rotating spicules also show flow along the rotation axis, so a spicule viewed perpendicular to the axis should also show sky plane motion or expansion. It is unknown if spicules form with rotational axes parallel to the surface, as our observations would require.

CHAPTER 6
NOISE MODELING

6.1 Introduction

I develop an image noise model for the *Multi Order Solar EUV Spectrograph* (*MOSES*) instrument. *MOSES* records images using 3 2048x1024 rear illuminated CCDs. Analog to digital conversion is 14 bit. I use the photon transfer curve method [14]. Each CCD was exposed to varying levels of visible light, and the noise characteristics were analyzed. Excellent agreement was found with a model that includes only Poisson distributed photon shot noise and gaussian distributed read out noise. This model is described by two parameters - the read out noise variance and the gain. The read noise variance is directly measured, and the gain is deduced from the noise statistics. Analysis is also made of the noise in image data obtained by [15] for estimation of the CCD flatfield variation. Nominal illumination wavelength for these images is 30.4 nm - *MOSES* operating wavelength. The noise in these appears smooth relative to the noise in the visible light images. This is characteristic of charge diffusion which is well known to occur in CCDs operating at UV to X ray wavelengths [14]. Using power spectral densities, I derive a kernel that describes the probability of the diffusion of photoelectrons to neighboring pixels. I conclude with a discussion of *MOSES* noise in wavelet transform space.

6.2 Theory

CCD operation relies on the photoelectric effect, where incident photons interact with lattice electrons to generate free electrons in the material. Electronic circuitry on the chip is used to produce a grid of potential wells, known as pixels, which trap the free electron at or near the location it was generated. The total charge collected in each pixel is then measured and converted to a digital number [DN]. The image produced by a CCD is an array of numbers, one for each pixel, whose values are proportional to the amount of charge collected in each pixel.

The idealized CCD is a linear system which converts some number of interacting photons P into a digital number S [DN], and is described by

$$S = G * \eta * P \tag{6.1}$$

The constant η is the quantum yield in $e^{-}/photon$, and is the number of free electrons generated as the result of a single photon/lattice interaction. For photons above 400 nm, the quantum yield is unity. For shorter wavelengths, free electrons may be produced with sufficient kinetic energy to free other lattice electrons, and $\eta > 1$. For extreme ultraviolet 30.4 nm photons interacting with silicon, $\eta = 11.12$ e-/photon. The constant G $[DN/e-]$ is the CCD gain, the analog to digital conversion constant from a number of electrons to DN. For simplicity I will use $\eta = 1$ unless otherwise noted.

Repeated measurements of S under identical exposure conditions will result in variation about a mean value $\bar{S}$. This variation is called noise. Under dark conditions, when the illuminating photon flux is zero, noise in the analog to digital (A/D) conversion process results in a fluctuation of S about zero (or more typically, a "pedestal" value greater than zero). This type of noise is called read out noise

and is well described by a gaussian distribution with variance σ_R^2 [DN]. In addition, free electrons are generated from thermal fluctuations in the CCD material, which produce measurable signal and consequently noise. This is called dark current, as signal is produced even under dark conditions, and the associated noise is Poisson distributed. At the operating temperature of *MOSES* CCDs dark current is effectively non existent, but is present in room temperature measurements.

Read out noise is the same for each pixel in the CCD, as the charge in each pixel is measured by a single A/D converter. In principle, the quantity σ_R^2 is determined by calculating the variance of a single short exposure, known as a bias exposure. In practice, bias frames taken at room temperature will be corrupted by dark current, whose associated noise will exceed the read noise component. An upper bound to the read noise is obtained from a room temperature bias frame, by calculating the variance of the first few rows of the image, which are read out first and thus have the least amount of time to accumulate dark current. The resulting estimate differs little from a similar value estimated from bias frames taken with a cooled CCD.

When exposed to light S also exhibits noise due to variation σ_P^2 in the number of photons which interact with the CCD in a particular exposure. The number of interacting photons, or counts, is described by a Poisson distribution. If the average number of interacting photons $\bar{P}$ is sufficiently great ($\bar{P}$ 10), the Poisson distribution is approximately gaussian with variance $\sigma_P^2 = \bar{P}$. This approximation becomes exact as $P \to \infty$. Dark current, if present, contributes signal with $\eta = 1$ and Poisson distributed noise, and is indistinguishable from signal generated by illuminating visible light photons.

Together, then, Poisson plus gaussian distributed noise sources constitute the basic noise model describing the variation in S:

$$\sigma_S^2 = G^2\sigma_P^2 + \sigma_R^2 \tag{6.2}$$

Given sufficient counts, $\sigma_P^2 = \bar{P}$, and from 6.1 $\bar{S} = G\bar{P}$, so

$$\sigma_S^2 = G\bar{S} + \sigma_R^2 \tag{6.3}$$

The unknowns on the RHS of 6.3 are G and σ_R^2. Once determined, the error (variance) on a measured pixel value $\bar{S}$ is simply determined from this linear equation. The quantities $\bar{S}$, σ_S^2, and σ_R^2 in 6.3 may all be calculated from direct measurement. It is possible to calculate these values for each pixel in the array, but a large volume of data must be collected in order to obtain good statistics. Alternatively, the statistics may be calculated over NxN arrays of adjacent pixels within a single CCD image taken under spatially uniform illumination. I chose the latter alternative given constraints on the volume of data that could be obtained with the *MOSES* without overloading the thermal capacity of the system.

In an ideal system, therefore, good statistics are obtainable from a single image and G is determined by rearranging 6.3. In practice, G itself varies somewhat from pixel to pixel. This variation is known as flatfield variation, so called because is is typically mapped using deep exposures with flat illumination. Flatfields were measured by Fox et al, using creativity to overcome lack of a flat EUV source. Flatfield variation is repeatable, not noise, but adds a variance term to 6.3 that goes as the square of $\bar{S}$ when statistics are taken over a group of adjacent pixels. For that matter, spatial variation in the illumination of the CCD will also generate such a term, and will dominate the linear term whose slope allows determination of G. These quadratic terms may be removed by differencing, pixel by pixel, two identical exposures. The

variance of this difference image is twice that of 6.3. In practice the estimate for G is improved by taking exposures at varying signal levels, from a bias exposure up through saturation, and fitting a line to the measured difference image variance less the read out noise variance.

6.3 Methods

6.3.1 Light Source

The CCDs were illuminated with specially designed LED light sources, which operate at 635 nm. The wavelength was chosen so that $\eta = 1$. The LEDs were mounted in a light tight tube, which was threaded into a flange which bolted directly to the filter tube mounting holes on the camera housing. Mounted in the tube between the CCD and the LED was an opal glass diffuser, designed to approximate a Lambertian source. The CCD/light source system is closed to outside light. The LEDs are controlled by a driving circuit which turned on the lights when triggered by the shutter open signal from the *MOSES* flight computer. The LED on signal is a square pulse, one per *MOSES* exposure, and the time interval is set with a function generator. Knowing the exact on time of the LED is not critical, but it is important that back to back exposures could be made with the same LED on time, so that the difference images have the signal variance given in 6.2.

6.3.2 Data

Data was collected on 2012 September 9. 10 bias exposures, exposure length 1 ms, were taken both at the beginning and the end of the experiment for measurement of read noise. Following the first 10 bias images, and prior to the last 10 bias images,

10 1 s darks exposures were taken for measurement of the image pedestal. The dark sequences were triggered by the "DARK" uplinks on the *MOSES* ground station - no shutter open signal is sent, so the LED sources are not activated. The light exposures were done with the"DATA START" uplink. The light exposure sequence consisted of two one second exposures, with two exposures per sequence for difference image generation. The LED on time was set with the function generator, with times ranging from 1 μs to 0.4 s. After setting the LED on time, the sequence was initiated, with two exposures per sequence, each exposure sending the shutter open signal which triggered the LEDs. After the sequence was complete, the LED on time was increased, and another sequence was run. These 55 exposures cover the full range of the CCD analog to digital conversion, from bias to full well. 55 sequences, with 2 exposures per sequence, and 3 CCDs results in 330 light images at varying signal levels. A sample image is shown in figure 6.1. The curve of signal variance versus signal is known as a photon transfer curve.

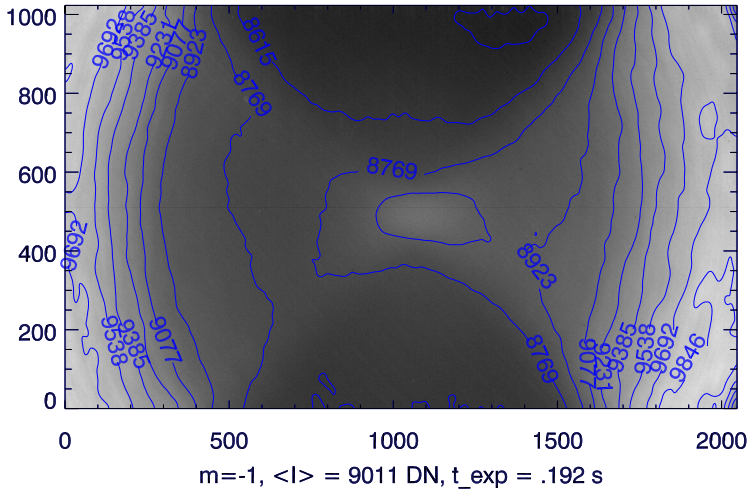


Figure 6.1: Image produced with the illumination device described in §6.3.1. This image is taken with the m=-1 CCD; the other CCD illumination patterns are similar in appearance.

6.4 Analysis

6.4.1 Read Noise and Pedestal Measurement

This experiment was performed at room temperature. Signal accrues in the CCD pixels at all times due to dark current, which is subject to shot noise and thus corrupts measurement of read out noise. Each CCD exposure consists of a flush, in which all charge is cleared from all pixels, integration of charge during the exposure time, followed by read out, where the accrued charge is converted to DN. The flush is a fast operation; all pixels are effectively zeroed at the same time. Read out, however, takes approximately four seconds. Each pixel is read sequentially, meaning the last pixel in the array has four seconds more time to accrue dark current. Thus, although the dark exposures were of 1 ms exposure time, the last rows to be read have an

effective exposure time of four seconds as far as dark current is concerned. Therefore read noise was estimated from the first two rows of the CCD to be read, giving 4096 pixels to produce statistics, with an effective exposure time of approximately 5 ms. For reasons similar to those described above, the image pedestal was measured using the first two rows of the 1 s dark exposures.

6.4.2 Signal Mean and Variance Measurement

Difference images were generated by taking the two light exposures at each LED on time, differencing them, and dividing by $\sqrt{2}$. The mean image was the average of the two images, less the pedestal. Estimates of the signal and variance were generated by calculating the mean and variance of NxN arrays within the images, centered at random locations. 1000 estimates were made for each LED on time. N was varied to investigate the effect of box size on the results.

6.5 Results

Results for each CCD are shown graphically in figures 6.2, 6.3, 6.4 for the m=-1, m=0, and m=+1 CCDs respectively. The data is plotted in log scale in order to show the variation in the curve in the read out noise regime. All three plots show a slope of 1 over the full A/D range after subtraction of the read out noise, indicating excellent agreement with the expected linear relationship between the mean signal and the signal variance. These curves show the mean signal and variance values generated using a box width of 45 pixels.

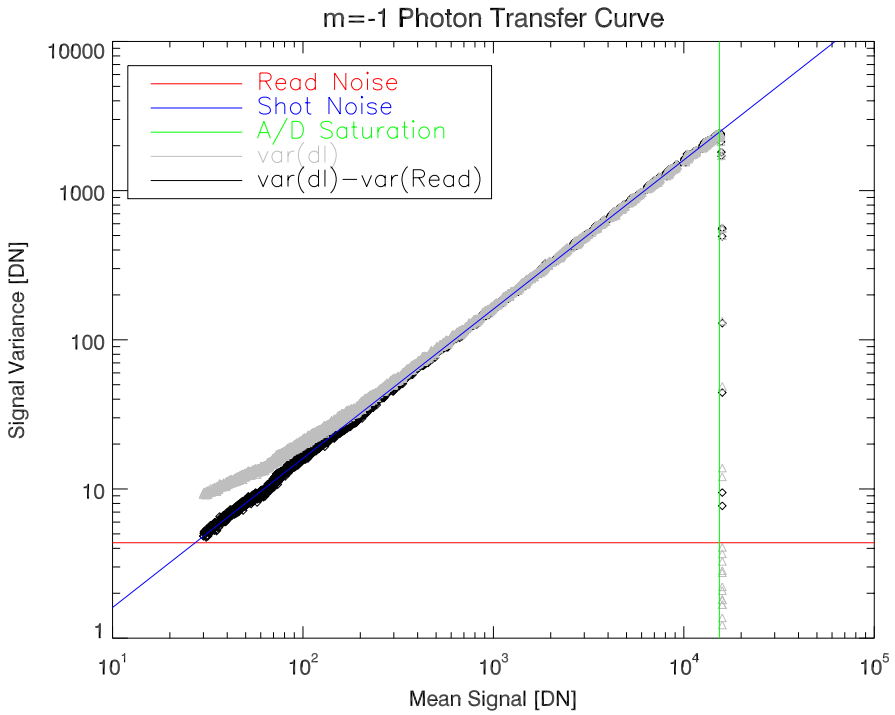


Figure 6.2: Photon transfer curve for m=-1 CCD. The data is plotted on log-log axes to show the various signal regimes. At low signal, the presence of read noise (magnitude of variance indicated by horizontal red line) results in a deviation of the transfer curve from unity slope (gray curve). At higher signal the read noise becomes insignificant compared to the Poisson distributed shot noise, and the curve takes on a characteristic slope of one, until A/D saturation is reached and the variance drops precipitously, as all pixel values approach 2^14-1 DN (vertical green line). When the read noise variance is subtracted from the total signal variance, the Poisson limited linear curve extends all the way to the zero signal level, indicating good estimation of the read noise variance. For reference the theoretical curve for pure Poisson noise is overplotted as a blue line of slope 1.

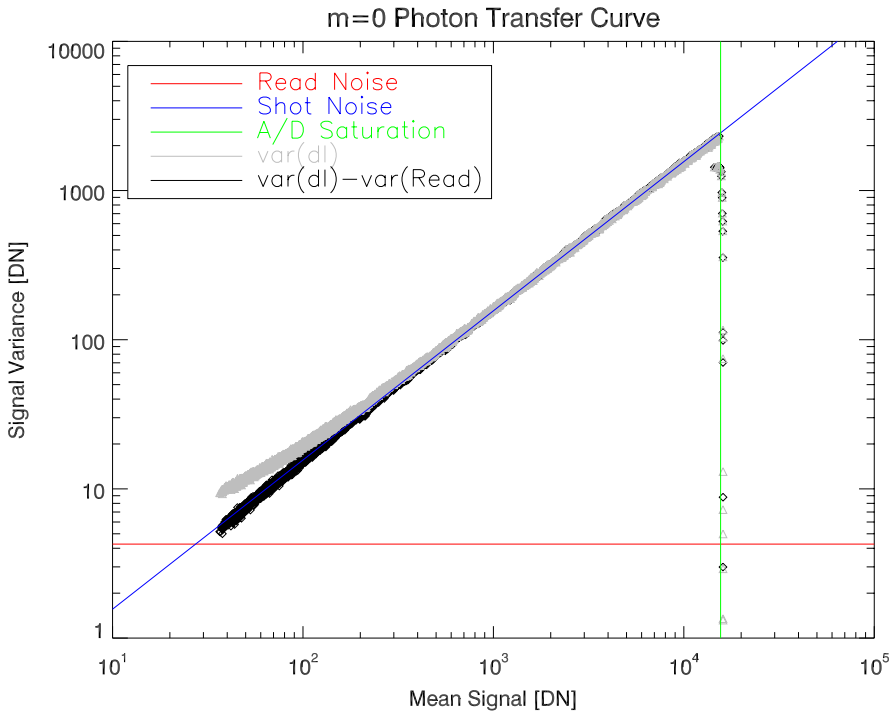


Figure 6.3: m=0 CCD Photon transfer curve. See figure 6.2 caption for further details.

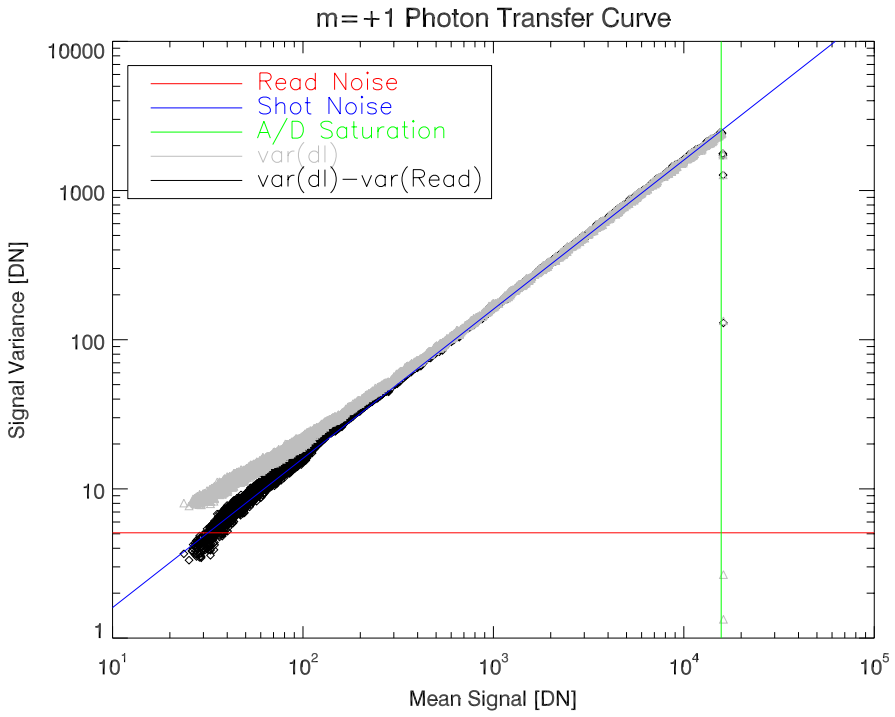


Figure 6.4: m=+1 Photon transfer curve. See figure 6.2 caption for further details.

The gain G is estimated by dividing the signal variance, less the read noise variance, by the signal mean. The read noise estimate is accurate, as after subtraction from the total variance the transfer curve becomes linear even at low signal (figures 6.2, 6.2 and 6.2); however, I choose to estimate the gain using data points where the signal is between the values of 5000 DN and 14000 DN. At these signals, read noise is negligible, so any effect read noise estimation errors on the gain estimation will be minimized. The upper bound keeps the estimates well below the region where the signal variance falls off due to A/D saturation. The gain estimates are shown graphically in figures 6.5, 6.6, 6.7 for m=-1, m=0, and m=1 respectively.

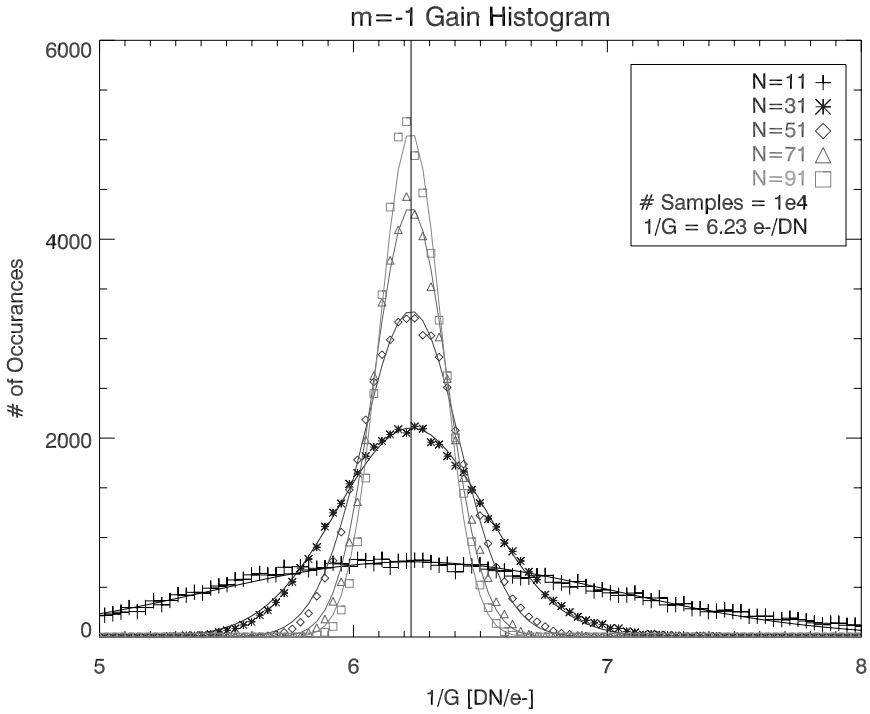


Figure 6.5: Histograms of estimated value of 1/G for the m=-1 CCD. The statistics are generated using NxN sub arrays of the noise images. As N is varied, the width of the histogram (which may be taken as an error estimate on the gain) varies, but the centroid remains the same. The symbols represent data, the solid lines are gaussian fits. The gain estimate results from averaging the centroids of the gaussian fits.

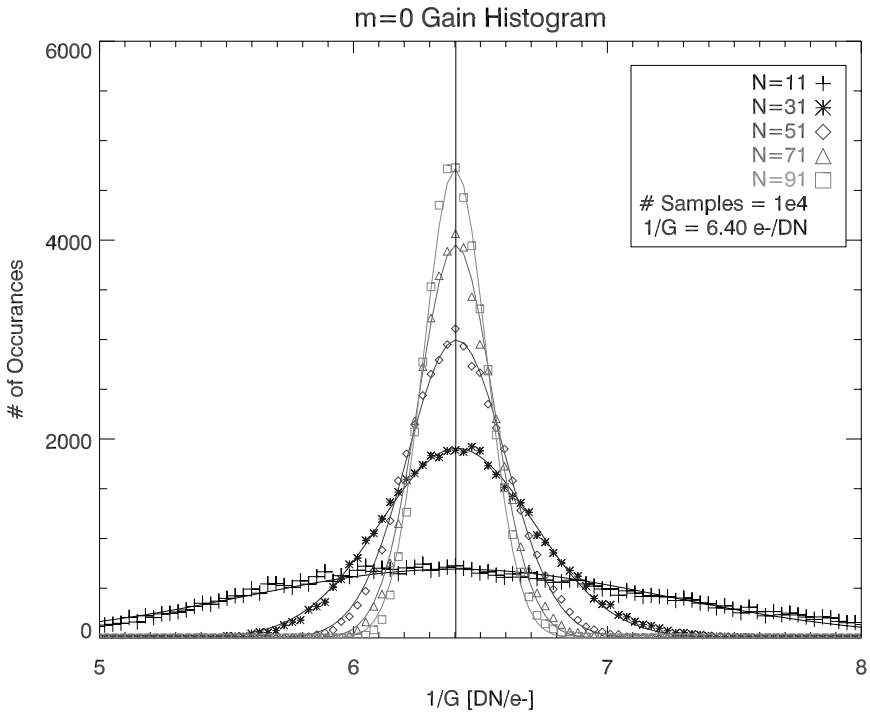


Figure 6.6: Histograms of estimated value of 1/G for the m=0 CCD. See caption of figure 6.5 for further details.

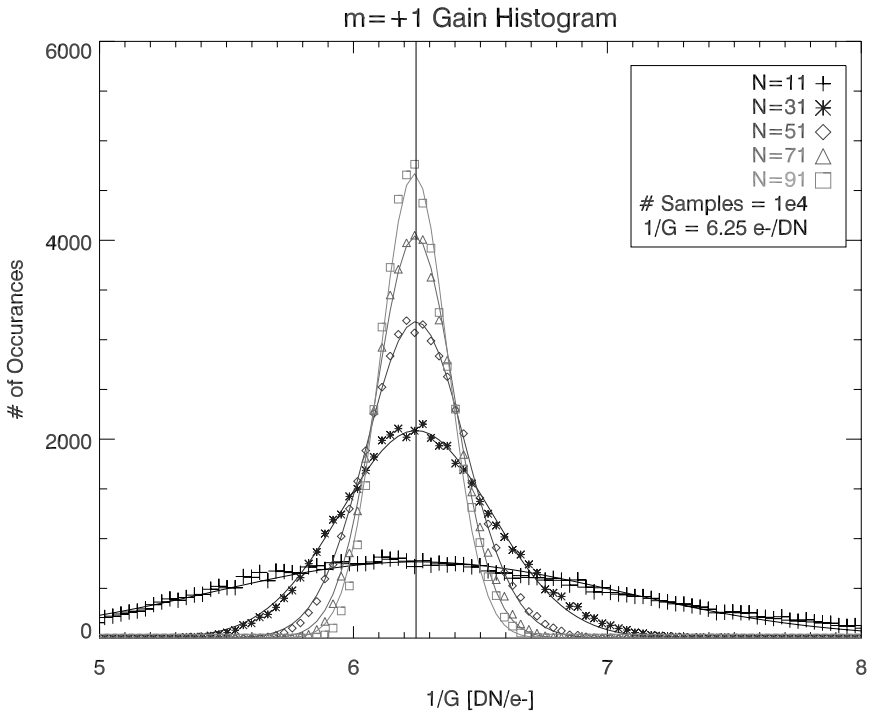


Figure 6.7: Histograms of estimated value of 1/G for the m=+1 CCD. See caption of figure 6.5 for further details.

The gain estimates are shown plotted as histograms. The different histograms correspond to different choices of box size in which the statistics were calculated. It is seen that box size affects the width of the histograms, but the centroid, which gives the gain, remains unchanged. The symbols represent measured histogram values; the solid lines are gaussian fits to the histograms. The gain histograms show a gaussian distribution, and the mean of the distribution is the estimate for the gain.

The measured noise in visible light is in excellent agreement with a model incorporating only photon shot noise and readout noise (i.e., eq. 6.3). This model is fully determined by the gain G and variance of the readout noise σ_R. The measured values of these parameters are given in table 1.

Table 1: Noise Model Parameters. See equation 6.3.

CCD	G [DN/e-]	$\sigma_R^2[DN]$
m=-1	0.161	4.4
m=0	0.156	4.3
m=+1	0.158	5.1

6.6 Noise at Operating Wavelength

[15] used an extreme ultraviolet source in combination with a nominal HeII 304 multilayer mirror to illuminate the *MOSES* CCDs at operating wavelength for measurement of the CCD pixel to pixel gain variation (flatfield). Metallic thin film filters were used to filter out visible light. These data are also useful for investigating the noise properties of the CCDs at operating wavelength. As noted above, one expected difference is the effective gain is different, as $\eta > 1$. For a wavelength of 30.4 nm, $\eta =$ 11.12 e-/photon. The effective gain, then, at this operating wavelength for, e.g., the m=-1 detector is $G_{EUV} = G\eta = 1.77$ DN/photon.

A typical image is shown in figure 6.8. Average exposure level is just over 10^4 DN, about 2/3 of the way to A/D saturation. This image is taken with the m=-1 detector. As above, the noise is accessed by differencing two images made under the same exposure conditions.

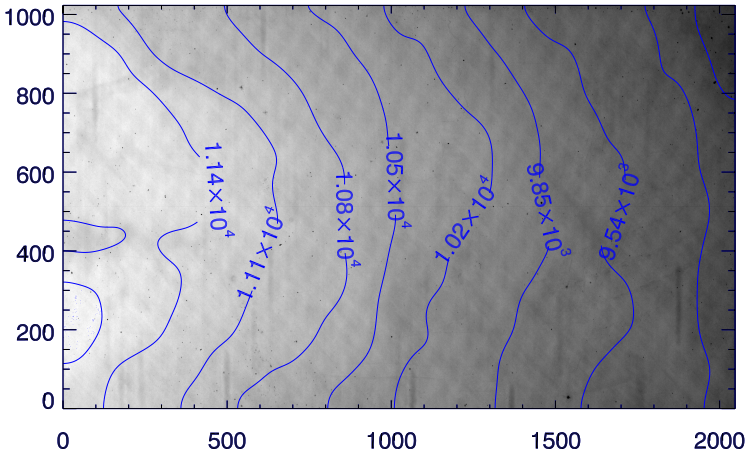


Figure 6.8: Image produced with EUV illumination of the m=-1 CCD; the other CCD illumination patterns are similar in appearance. The contours are smoothed. The underlying grid pattern is produced by the thin metallic filter used to block visible light.

Comparison of the noise in the visible light images and the EUV images is facilitated by use of the generalized Anscombe transformation ([16], [17]). Application of this transformation to an image containing (signal dependent) Poisson noise plus gaussian distributed read noise results in a new image, whose noise is gaussian distributed with standard deviation of 1. The Anscombe transformation is applied to the images prior to differencing, then the standard difference image is computed. The gain used for the visible light images (m=-1 detector) is that from table 1; the gain used for the EUV data is G_{EUV}.

Figure 6.9 shows overlapped 128x128 pixel sub images extracted from the noise from from the (Anscombe transformed) EUV data (lower left), (Anscombe trans-

formed) visible light data (center), and a gaussian distributed noise image, standard deviation 1, generated with a random number generator (synthetic noise).

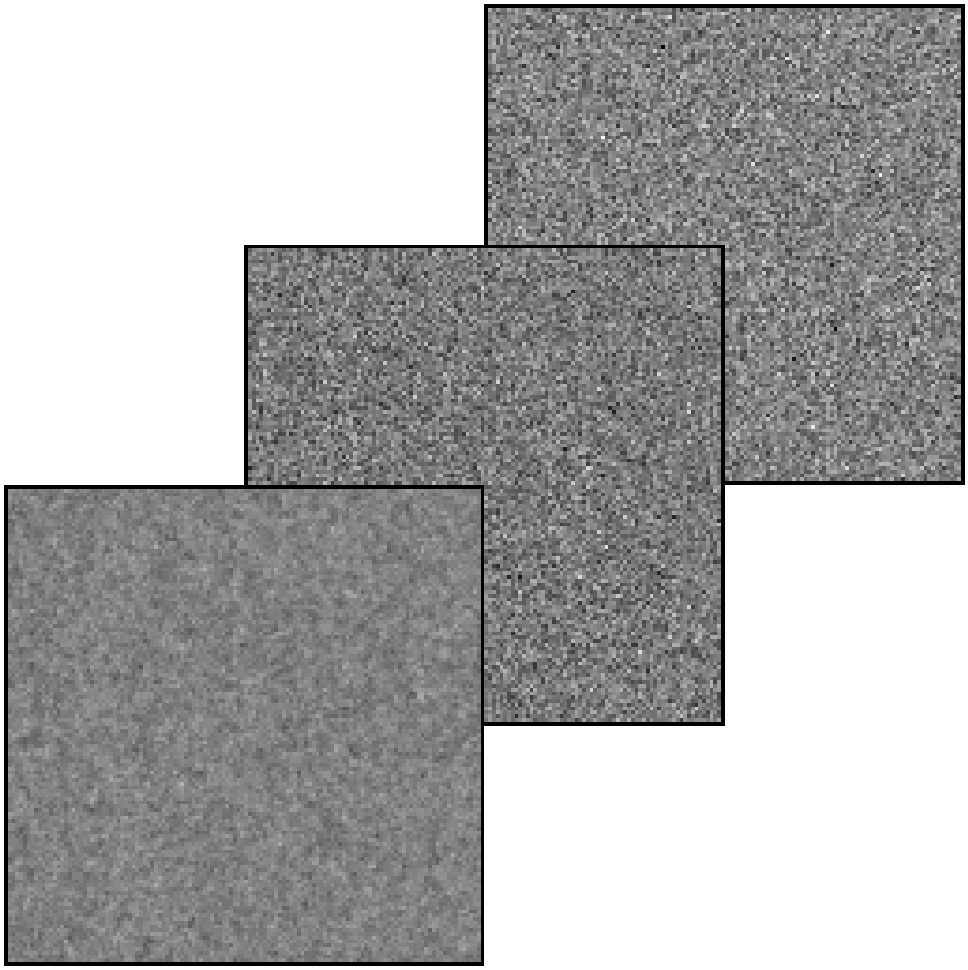


Figure 6.9: Noise from various sources: Synthetic (upper right), visible light measurement, m=-1 CCD (center), and EUV measurement, m=-1 CCD (lower left). All noise images are displayed on the same scale.

The noise from the visible light data appears identical to the synthetic noise; the EUV noise appears to have been smoothed. This is likely due to imperfect charge collection efficiency at EUV wavelengths [14]. The *MOSES* CCDs are rear illuminated devices. For a variety of reasons it is impractical or not possible for the electric fields

which define the pixel volumes to extend to the rear (illuminated) surface of the device, leading to a thin layer of field free material. The depth at which a typical EUV photon/electron interaction occurs is also very shallow, thus many interactions occur in the field free regions. Electrons which are excited in the field free region will random walk through the material, until by chance they encounter the electric field defining a pixel and are captured. As lateral movement may occur in this walk the capturing pixel may not be the one closest to the site of excitation. This imperfect charge collection efficiency is sometimes referred to as charge diffusion or charge spreading. This is investigated in the following msusections, first using power spectra derived with the Fourier transform. Subsequently the noise properties are examined in wavelet space.

6.6.1 Noise Power Spectra

Power spectra are estimated from the noise as the absolute square of the Fourier transform of 128x128 pixel sub images drawn from random locations in the noise images. 1000 power spectra are estimated from each noise source and averaged to reduce noise in the estimated power spectra. These power spectra are shown in figure 6.10.

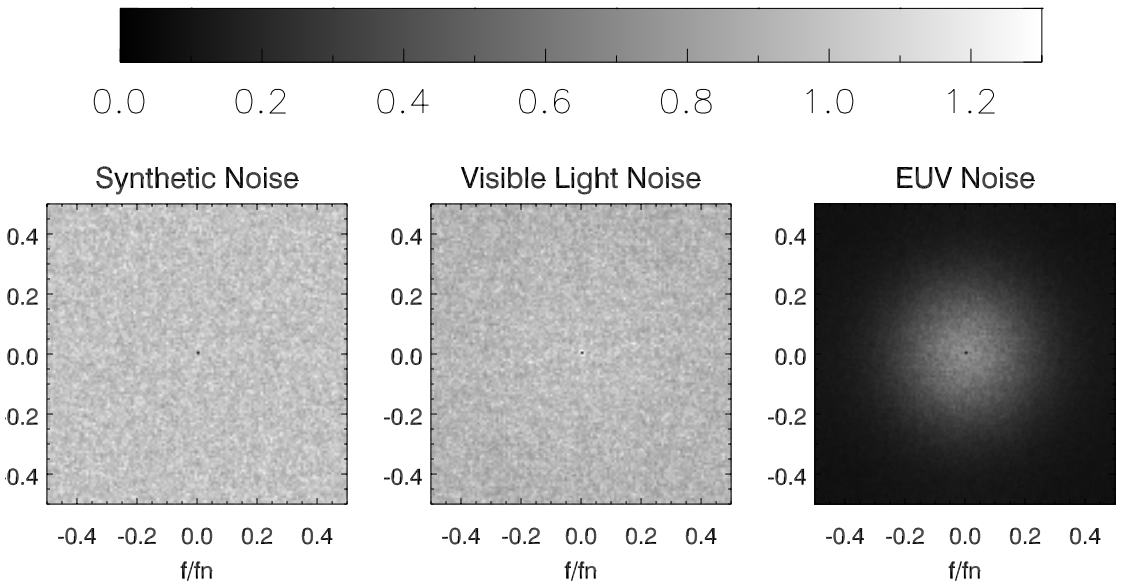


Figure 6.10: Power spectral densities of noise from synthetic (left), visible light (center), and EUV (right) data. All panels are displayed with the same scale.

The synthetic, gaussian distributed noise has equal power at all frequencies, a property referred to as white noise. The visible light noise appears to share a white noise spectrum; the EUV noise, however, falls of isotropically as the magnitude of the frequency increases. This type of noise is referred to as red noise, as more power exists at low frequencies, and is most likely the result of charge diffusion at EUV wavelengths.

It is possible to attribute a smoothing kernel to this power spectrum. The interpretation of this kernel is the probability that an electron will be captured by a pixel in the neighborhood of the pixel nearest the interaction site. If randomly distributed noise ϵ is convolved with smoothing kernel κ, the power spectrum of the result is

$PS = |\tilde{\epsilon}|^2|\tilde{\kappa}|^2$. If the initial noise has a white power spectrum then $|\tilde{\epsilon}|^2 = 1$, and the power spectrum of the smoothed noise is equal to the power spectrum of the kernel. Given the interpretation of the kernel it must be real, and I assume it is symmetric; such a kernel has a real Fourier transform, which is equal to the square root of its power spectrum, i.e., $\tilde{\kappa} = \sqrt{PS}$. Following this logic, the charge diffusion kernel is estimated by inverse transforming the square root of the EUV power spectrum. Very few pixels of the result differ appreciably from zero; a 3x3 kernel is sufficient to describe the diffusion. The kernel is normalized to sum to 1 as befits a probability distribution. The values of the charge diffusion kernel are shown in table 2.

Table 2: Charge Diffusion Kernel κ. Values represent the probability of a free electron being captured by a pixel in the neighborhood of the interaction site.

.034	.077	.034
.076	.558	.076
.034	.077	.034

6.6.2 EUV Noise in Wavelet Space

The wavelet transform is extremely useful for image processing where features of various size scales exist at well defined locations, as is typical for images of real world scenes, and therefore it is useful to discuss noise in the context of wavelets. Given discrete (pixellated) data, of interest is the discrete wavelet transform. The particular algorithm used here is the Atrous discrete wavelet transform. Other algorithms would result in different numbers, but the same analysis may be applied.

Application of the Atrous transform to an LxM size image results in an LxMxN array, consisting of N-1 wavelet coefficient images and one smoothed image. The

original image is recovered exactly by summing over the N dimension. In the presence of noise, the wavelet coefficients are randomly distributed about the true value, with the distribution based on the noise present in the image. Knowledge of the noise in wavelet space allows significance testing of coefficients, which is useful in wavelet noise reduction, deconvolution regularization, and other applications where one might wish to know whether a coefficient is indicative of real signal, or has arisen from random noise.

Wavelet coefficient significance levels are determined by the noise present in the data. The Anscombe transformation and generalizations thereof may be used to transform signal dependent (e.g., Poisson) noise present in the data to uniformly distributed gaussian noise. In such cases, the distribution of wavelet coefficients due to the noise is determined by applying the wavelet transform to uniform gaussian noise, and calculating the standard deviations σ_j of the coefficients at each scale j. Significance testing is carried out by comparing the wavelet coefficients of the Anscombe transformed data to the σ_j. Coefficients whose magnitudes are sufficiently in excess of σ_j can be said to indicate real signal, rather that having arisen from the noise.

In the presence of charge diffusion, I assume that a.) the A/D gain measured in visible light is correct, and b.) that the charge diffusion kernel is independent of signal level. Under these assumptions the significance levels are determined as above, with the wavelet transform applied to the Anscombe transformed EUV noise from §6.6, using G_{EUV} for the CCD gain.

The significance levels are shown in figure 6.11 for uniform gaussian noise, (Anscombe transformed) visible light noise, and (Anscombe transformed) EUV noise.

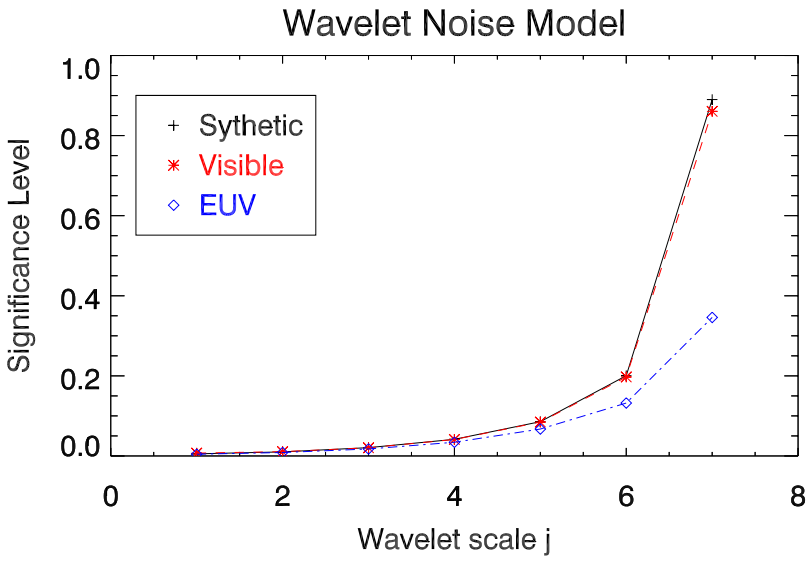


Figure 6.11: Significance levels as function of wavelet scale for the Atrous transform applied to different noise sources. The significance levels are reduced in the EUV data, as the noise is smoothed due to charge diffusion. Note that signal to noise does not increase, as the signal is smoothed accordingly.

Unlike the Fourier space power spectrum, white noise in wavelet space has increased variance at small scales, and decreases at larger scales. The Anscombe transformed visible light data shows the same significance levels as the synthetic noise, as indeed, it has been transformed into uniformly distributed gaussian noise. Of most interest for *MOSES* data analysis is the significance levels measured from the EUV noise, where charge diffusion results in lower variance in the noise at small scales, tracking again with the gaussian noise at larger scales. It is important to point out that this reduced variance does not improve detection, as the charge diffusion that smooths the noise also smooths the image signal, reducing intensity and sharpness of small scale image features.

This analysis was carried out for all three detectors. The 1-σ significance levels of Anscombe transformed *MOSES* data under the Atrous transformation for each detector are shown in table 3.

Table 3: Wavelet space significance levels from the Atrous transform. Size scale decreases as j increases.

j	m=-1	m=0	m=+1
1	.005	.005	.005
2	.01	.01	.01
3	.019	.019	.019
4	.037	.037	.037
5	.073	.073	.074
6	0.14	0.14	0.14
7	0.37	0.35	0.36

CHAPTER 7

MOSES-I POINT SPREAD FUNCTIONS

7.1 Introduction

The *Multi-Order Solar EUV Spectrograph*(*MOSES*) ([11]) is designed for slitless imaging spectroscopy of the solar transition region. Co-temporal image and spectral information are obtained over a wide field of view by recording images $\mathcal{I}_m$ at three spectral orders $m = -1$, $m = 0$, and $m = +1$ of a concave diffraction grating. Spectra are recovered through a tomographic inversion.

[15] noticed significant differences between the point spread functions in each order, and discussed the potential for systematic error. The problem is discussed further in chapter 8. A reasonable estimate for the core of the point spread functions would at minimum contribute to understanding the propagation of systematic errors in *MOSES* inversions. Better, the estimates could be incorporated into the inversion algorithm to achieve reduced error and improve spatial and spectral resolution.

Features exist at a range of size scales and shapes in the *MOSES* data, but the smallest features in the image in a given order all take on very similar shape. I will argue that these features are unresolved, and the shapes are representative of the core of the point spread function in that order. Inspection of the full data sequence indicates gradual time variation in the point spread functions over the 5 minute flight.

$\mathcal{I}_0$ abounds with unresolved features, and the point spread function is easy to see. Unresolved features are more difficult to find in the dispersed orders $\mathcal{I}_{-1}$ and $\mathcal{I}_{+1}$ as many compact features have strongly doppler shifted spectra (see chapter 5). A feature must be unresolved both spatially and spectrally for the point spread

function to govern the shape. Such features exist in the data; they may be examples of transition region blinkers ([18]).

In this paper I use wavelet methods to estimate *MOSES* point spread functions directly from the data. Wavelet methods are described in §7.2, point spread function estimates in §7.4, and deconvolution in §7.5.

7.2 Wavelet Methods

The wavelet transform has been applied to many problems in image and signal processing. As the Fourier transform is used to analyze frequency content in periodic data, the wavelet transform is suitable for analysis of data in which features of interest are localized in both position and size. The wavelet transform applied to pixellated data is referred to as the discrete wavelet transform. Many algorithm choices exist when computing the discrete wavelet transform. I've chosen to use the particular algorithm known as the à trous transform.

7.2.1 à trous Discrete Wavelet Transform

The à trous transform ([19],[20]) proceeds by application of a low pass filter to $\mathcal{I}$ resulting in the smoothed image $\mathcal{I}_s$. The smoothing kernel elements are the B_3 spline coefficients.

The difference images $w = \mathcal{I} - \mathcal{I}_s$ are the wavelet coefficients, which represent variability in the image that was lost upon passage from $\mathcal{I}$ to $\mathcal{I}_s$. This lost variability exists in the image within a specific range of spatial size scales. Wavelet coefficients from the à trous transform have mean zero averaged over the image.

Wavelet coefficients representing successively larger image spatial scales are calculated by iterative application, with $\mathcal{I}_s \rightarrow \mathcal{I}$ and halving the filter cutoff frequency at each iteration. Results of the transform up scale N are a set of wavelet coefficient images $w^j, j = 1..N$, where scale increases with j, and the final smoothed image $\mathcal{I}_s^N$. The original image is exactly obtained by $\mathcal{I} = \mathcal{I}_s^N + \sum_j w^j$. $\mathcal{I}_s^N$ and the w^j have the same dimensions as $\mathcal{I}$ (no decimation). A tilde over an image will be used to denote the à trous transform of that image.

7.2.2 Significance Testing

The wavelet coefficients of a noisy image are noisy. When working with noisy images, statistical significance testing can be done on the w^j to differentiate signal from noise. The utility of this resides the fact that noise typically exists at all image scales, whereas an image feature often occupies only a small range of scales. Whether a coefficient is determined to be significant depends on the amplitude of the coefficient relative to possible values given the image noise distribution.

MOSES images show Poisson distributed photon shot noise plus gaussian distributed read out noise (chapter 6). Signal independent wavelet significance testing of images with this signal dependent noise model is facilitated with the Anscombe transformation [Anscombe] $\mathcal{I} \rightarrow \hat{\mathcal{I}}$. Similar to square root scaling, with the detector gain accounted for, results in an image whose noise is uniform additive gaussian distributed. The distribution of wavelet coefficients of gaussian noise is gaussian, with standard deviation σ_j at the jth scale.

Significant wavelet coefficients of image $\mathcal{I}$ are determined from $\hat{\mathcal{I}}$. I adopt the hard threshold of $3\sigma_j$. If $|\tilde{\hat{\mathcal{I}}}(x, y, j)| > 3\sigma_j$ then $\tilde{\mathcal{I}}(x, y, j)$ is significant, and assumed

to indicate real signal in the data. If $|\tilde{\hat{\mathcal{I}}}(x,y,j)| < 3\sigma_j$ then $\tilde{\mathcal{I}}(x,y,j)$ may have arisen from the noise and is said to be insignificant.

7.2.3 Partial Reconstruction

Wavelet methods have been used to reconstruct objects within an image based on a subset of image wavelet coefficients [Bijouai]. This success of this approach reflects the fact that many objects are sparse in wavelet space. An object is generally described by a local maxima among positive, significant coefficients in wavelet space. Significant wavelet coefficients which are connected to the maxima in both scale and space are part of the same object. The object coefficients therefore occupy a volume in wavelet space.

The goal of partial reconstruction is to create an image whose wavelet coefficients are the same as those of the object, within the volume on which the object is defined. If the reconstructed image is p, the object coefficients are $\tilde{q}$, and A is the operator which transforms p and projects the result onto the support of $\tilde{q}$, the partial reconstruction problem is minimization of $||Ap - \tilde{q}||$. Solution method is iterative, beginning with $q(x,y) = 0$:

1. Calculate Ap $= \tilde{p}(x,y,j)$
2. Determine the additive error in the coefficients on the support of the object: $\tilde{\epsilon} = \tilde{p} - \tilde{q}$
3. Threshold $\tilde{\epsilon}$; retain only significant coefficients.
4. Calculate correction $\epsilon(x,y) = A^{-1}\tilde{\epsilon}$
5. Update $p = p + \epsilon$

6. Threshold $p > 0$

7. Repeat from steps 1 through 6. Iterations end when no significant coefficients may be found in $\tilde{\epsilon}$

The operator A^{-1} is inverse to the operation A. A projects an image into a list of wavelet coefficients; A^{-1} back projects a list of wavelet coefficients into an image. See [Bijaoui]. Step 3 was added as a wavelet based goodness of fit criterion.

7.3 Data

The data are from 2006 February 8 flight of *MOSES*. Images have been dark subtracted, corrected for flat field, cleaned of cosmic ray hits, and coaligned. Figure 7.1 shows a full $\mathcal{I}_0$ image, overlaid with regions of interest. The field of view in the red square and its wavelet decomposition are shown in figure 7.2. The green boxes indicate the locations of numerous compact sources in this image, shown in figure 7.9 in §7.8.

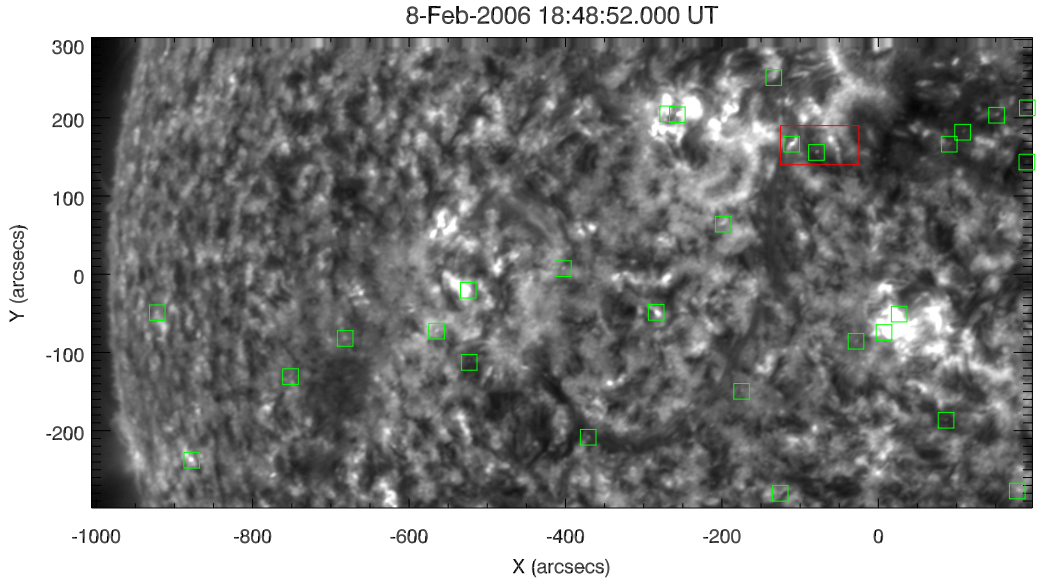


Figure 7.1: Context image. Full *MOSES* field of view. Over plotted, the red square is shown close up in figure 7.2. The green squares indicate the compact sources shown in figure 7.9.

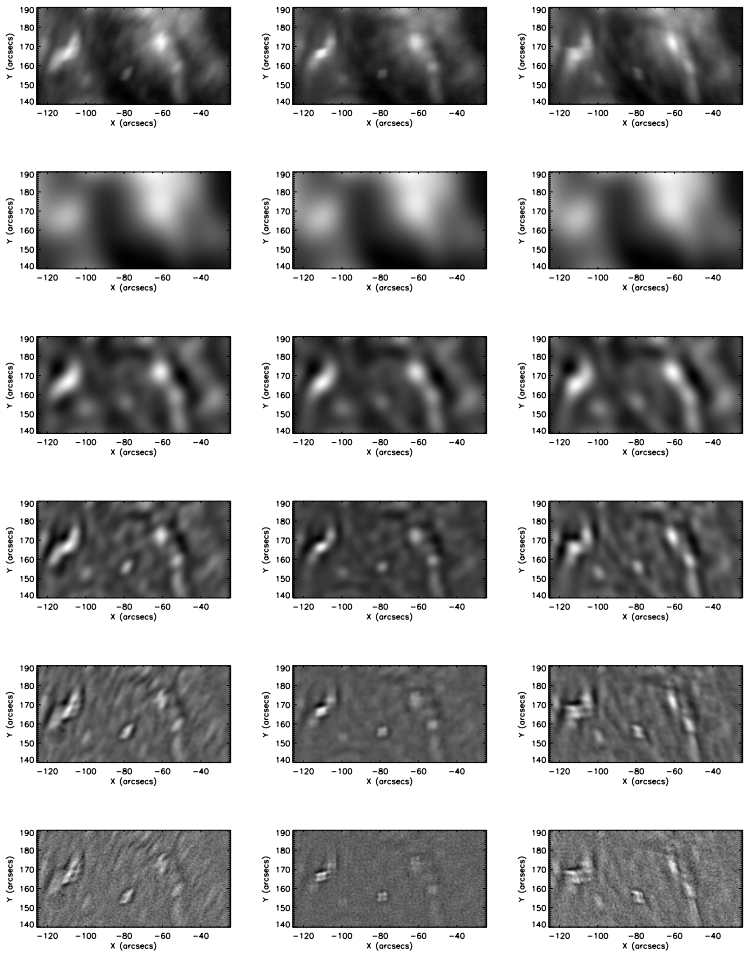


Figure 7.2: Close up of the region bounded in red in figure 7.1, and its wavelet transform up to scale 4. Original images top row, m=-1,0,1 left to right. Wavelet residual (smoothed images $\mathcal{I}_s^N$) second row. Wavelet scales 4 through 1 are third through last rows. The bright object center left was the subject of a paper by [FOX ApJ]. The shape of the core is dominated by the instrument point spread function, as is the compact source just below center frame.

The features in figure 7.2 clearly show the influence of the instrument point spread functions, particularly the bright core in the object center left and the compact object just below center. The imaging elements, different in each image – right leaning slash in $\mathcal{I}_{-1}$, rectangular shape in $\mathcal{I}_0$, and left leaning slash in $\mathcal{I}_{+1}$, are seen all over the images (see §7.8), and gradually change with time (see §7.6)

7.4 PSF Results

An appropriate image feature was selected for point spread function estimation. The feature is long lived, lasting at least 15 exposures with minimal change in appearance and no strong spectral signatures. The object was defined in the first two wavelet scales. The reconstruction results for each spectral order are shown in figures 7.3-7.5. Estimates are made from a single exposure, taken midway during the flight.

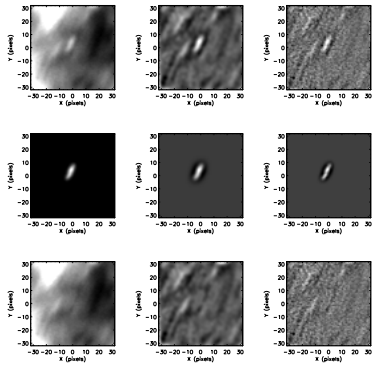


Figure 7.3: Reconstruction of a compact source for point spread function estimation, m=-1 spectral order. Each row shows an image on left, with the first and second wavelet scales to the right. Top row: original image. Middle Row: Extracted object/point spread function estimate. Bottom Row: Original image minus object.

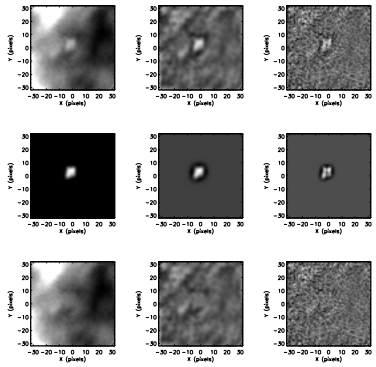


Figure 7.4: Reconstruction of a compact source for point spread function estimation, m=0 spectral order. Each row shows an image on left, with the first and second wavelet scales to the right. Top row: original image. Middle Row: Extracted object/point spread function estimate. Bottom Row: Original image minus object.

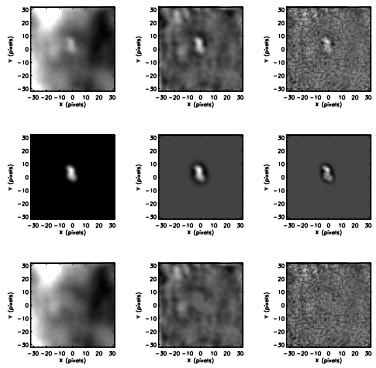


Figure 7.5: Reconstruction of a compact source for point spread function estimation, m=+1 spectral order. Each row shows an image on left, with the first and second wavelet scales to the right. Top row: original image. Middle Row: Extracted object/point spread function estimate. Bottom Row: Original image minus object.

The reconstruction algorithm works very well, resulting in smooth reconstructions which are consistent with the noise in the images. Full width half max of the point spread function estimates are approximately 6 pixels in each order. This is well in excess of *MOSES* design resolution. The size and shapes of the point spread functions are consistent with significant defocus. This combined with the design astigmatism in the dispersed orders (spherical mirror imaging off axis) results in the slashed appearance of those point spread functions. Six pixels corresponds to approximately 3.5" spatial resolution or 180 km s^{-1} spectral resolution, approximately equivalent to the with of spectra in explosive events ([2]).

7.5 Deconvolution

I've chosen to use the Richardson Lucy deconvolution method ([21],[22]) with wavelet based noise suppression ([17]). At each iteration the residuals are tested for significance. Pixels in the reconstruction are only modified if a statistically significant residual exists at that location. Iterations cease when the change in the residual between subsequent iterations drops below 10^{-3}. Average exposures take approximately 20 iterations, less for shorter exposures and more for longer exposures. Figure 7.6 recreates figure 7.2 using deconvolved image data.

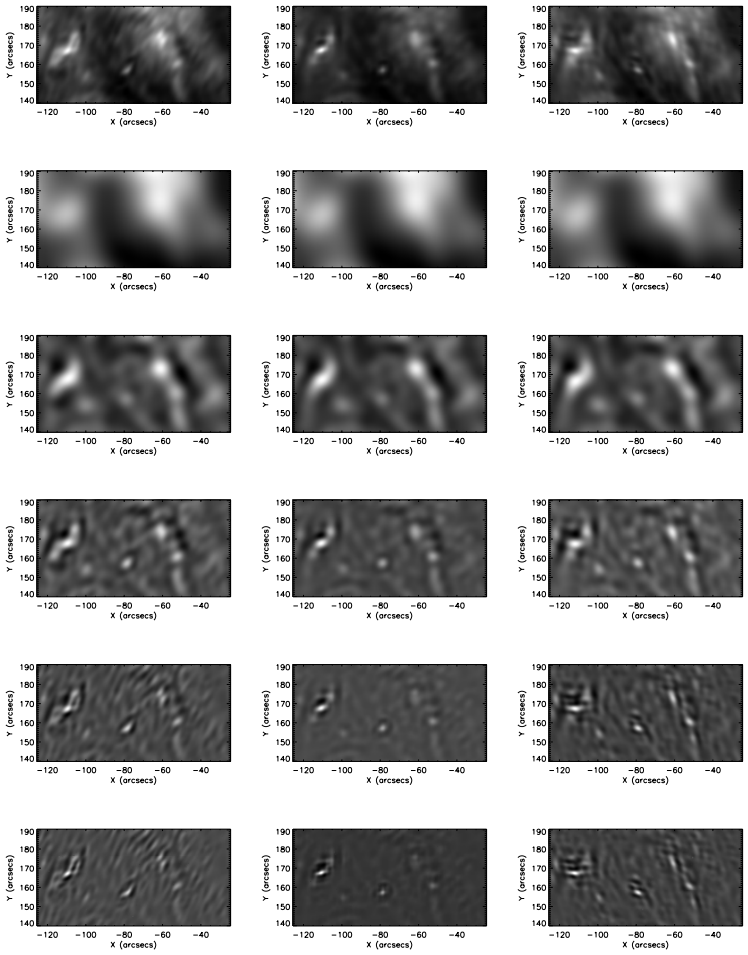


Figure 7.6: THESE DECONVOLUTION RESULTS ARE INCORRECT - NEED TO UPDATE THIS FIGURE.

The deconvolution significantly tightens up compact sources. Results of the deconvolution on the compact sources in figure 7.1 are shown in §7.8.

7.6 Temporal Variation

Examination of a time series of compact sources shows that the point spread functions change over the course of the five minute flight. This may be a thermal

expansion effect. Figures 7.7 and 7.8 show a time series of $\mathcal{I}_0$, centered on the small active region in *MOSES* field of view, pre and post deconvolution. The point spread functions estimated in §7.4 are used for all deconvolutions.

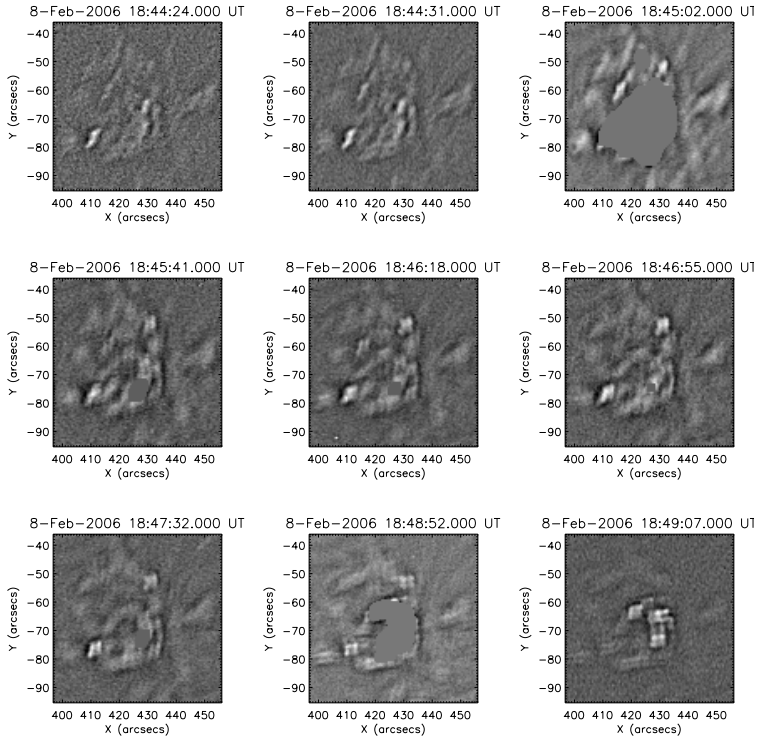


Figure 7.7: The small active region, $\mathcal{I}_0$ data scale 1 wavelet coefficients. Each frame is at a different time, covering most of the flight with time increasing from upper left to lower right. All bright compact objects in the field of view share the same shape, which evolves over the flight. This point spread function variability may be due to thermal expansion effects. Exposures numbers are 1, 2, 4, 6, 10, 14, 18, 23 and 25, of 27 total, going in order from upper left, left to right, top to bottom. UT shown in the titles of the individual panels.

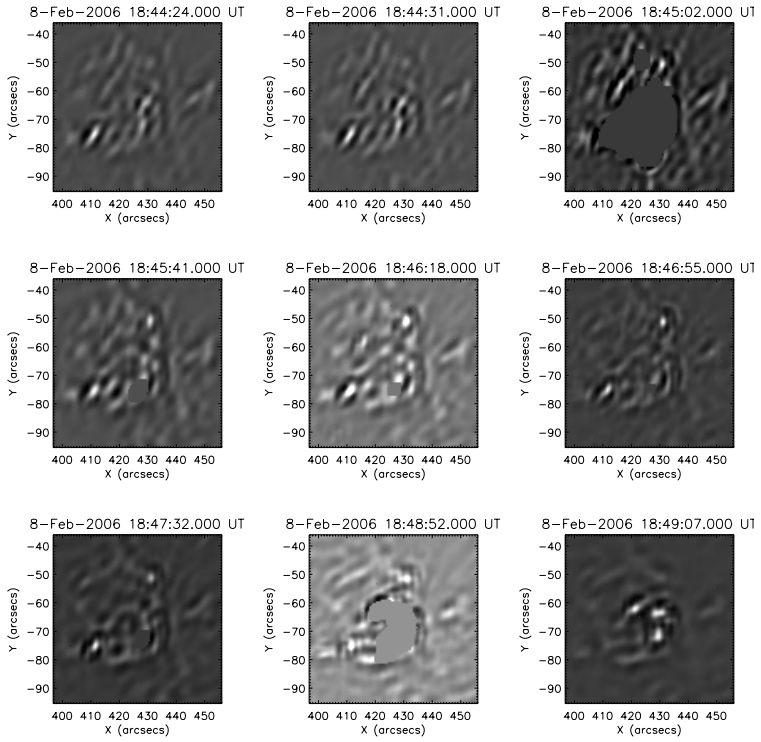


Figure 7.8: Same as figure 7.7, using the deconvolved data. The estimated point spread function (figure 7.4, left middle) is not ideal for early exposures. Significant resolution improvement is seen starting in the middle row (1/3 of the way through flight). It is not clear why the bottom center panel appears to suffer from increased ringing relative to the other images; otherwise, the deconvolution results towards the end of the flight are excellent.

Clearly using a single set of point spread functions suffer shortcomings early in the flight, but from exposure 6 on good results are simply achieved.

7.7 Conclusion

Repeated patterns observed in in small scale coefficients of wavelet transformed *MOSES* image data can be explained only as artifacts due to the image point spread functions. Suitable compact, isolated sources exist in the data that are extracted via partial reconstruction from wavelet coefficients, yielding estimates for the image point spread functions. Point spread functions exceed instrument resolution specification by a large margin. The point spread function morphologies are consistent with telescope defocus, combined with design astigmatism.

It may be possible to improve the results of *MOSES* data inversion by incorporating the point spread functions. Above I've shown the Richardson Lucy deconvolution applied to the data using the estimated point spread functions. The deconvolution incorporates wavelet based significance testing of residuals to reduce noise amplification. While it is generally impossible to say that a deconvolution has produced the "correct" results, the deconvolution results are smooth, show much tighter intensity distributions, and ringing is not excessive.

Time variance is seen in the point spread functions, probably the result of thermal expansion in the optical system upon exposure to sunlight. The change in point spread function is most rapid during the first quarter of the flight; subsequent changes are more subtle. The estimated point spread functions, from mid flight, are not ideal for early flight exposures. Although not presented here, it is possible to identify compact sources from early flight, where another point spread function estimate may be made.

A point spread function for each exposure might be useful. However, given the other sources of uncertainty – deconvolution, inversion, the underlying spectra of the source used for the estimate in the dispersed orders – it is convenient to proceed with a single set of point spread functions, as presented above.

7.8 Appendix

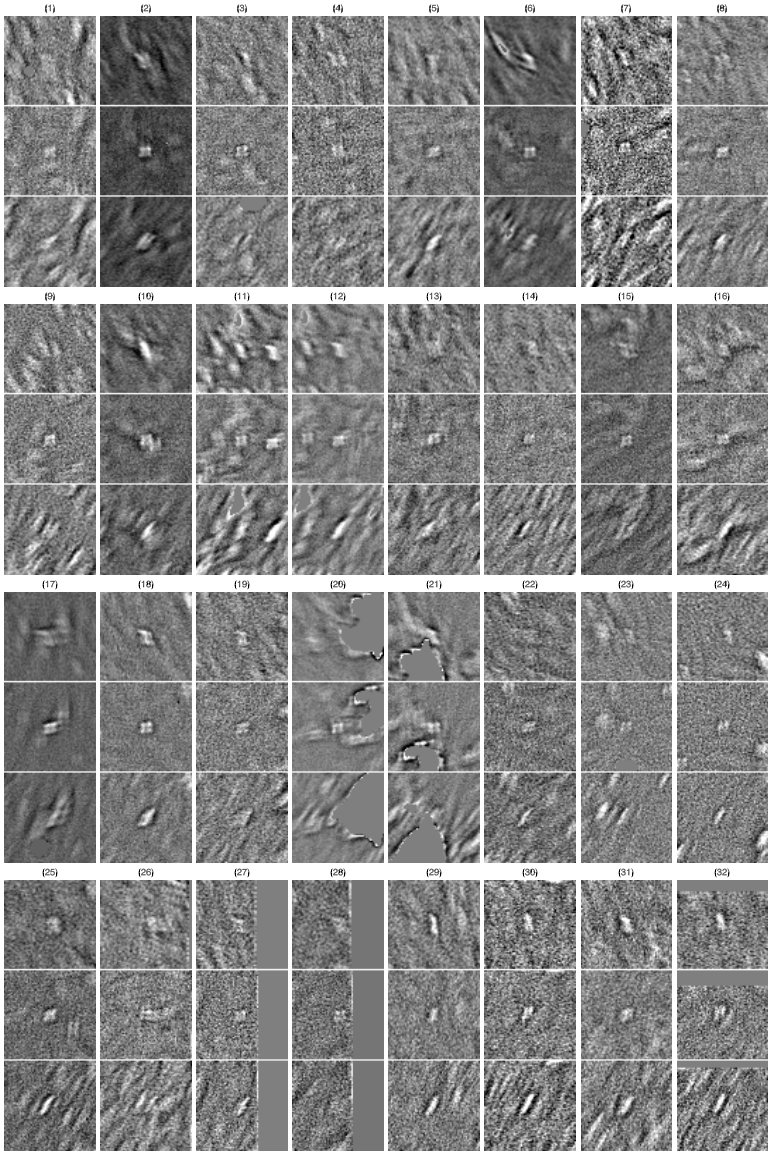


Figure 7.9: Compact objects in *MOSES* data, scale 1 wavelet coefficients shown; locations shown in green in figure 7.1. Each panel has three frames, top to bottom shows m=+1, m=0, and m=-1 data. The shape of the object is very similar from panel to panel in $\mathcal{I}_0$, but sometimes shows strong variation in the dispersed orders due to doppler shifted emission.

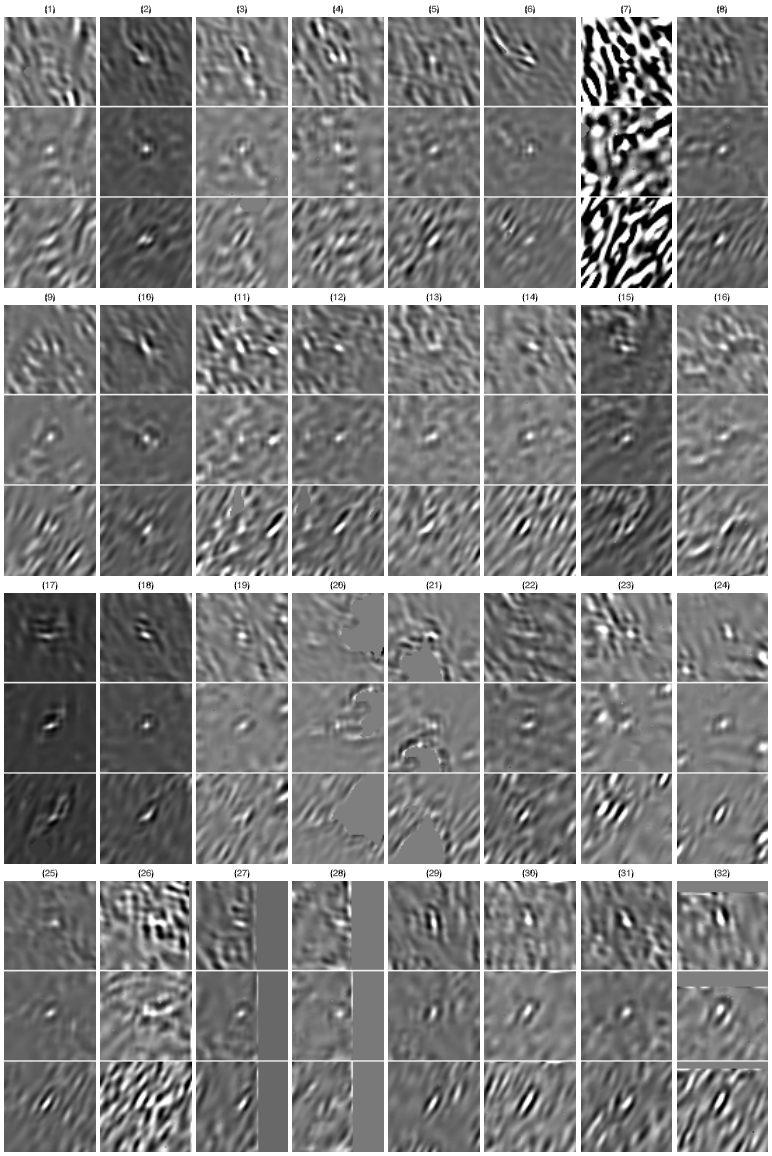


Figure 7.10: Compact objects in *MOSES* data from figure 7.9 after deconvolution. Scale 1 wavelet coefficients shown.

CHAPTER 8

MOSES INVERSIONS

8.1 introduction

Algebraic reconstruction techniques (ART) were introduced by ([23]). Under simple assumptions relating to the way the projections are approximated the tomography problem is reduced to the solution of a set of linear algebraic equations. Solution of the equations is done using the Kacmarz method, in which corrections are iteratively applied to an initial guess based on the disparity between the data and projections of the guess. Two correction methods were proposed, one using additive correction and one using multiplicative correction (MART). The additive correction is based on the difference between the data and projections; the multiplicative method uses ratios. In each case, corrections were applied sequentially, one projection angle at a time. MART algorithms naturally result in all positive values for the reconstructed array; the additive methods can be made so by thresholding negative values in the reconstruction.

The success of the original ART techniques were questioned by ([24]). He pointed out that generally reconstructions were substantially worse than those presented. Gordon's reconstructions were based on simulated projection data generated using the same numerical projection procedure used in the ART iteration, resulting in an internally consistent set of equations.

Gilbert demonstrated that ART are sensitive to inconsistencies in the set of projection equations. These inconsistencies arise in real data due to, e.g., noise in the measurement process. In the absence of noise inconsistencies arise due to the approx-

imations made in discretization of projection process itself. Reconstructions made based on more realistic projection data show salt and pepper artifacts which increase with iteration, despite convergence between the data and guess projections.

Gilbert proposed the simultaneous iterative reconstruction technique (SIRT). The correction to each pixel in the guess is based again on the disparity between the data and projections of the guess. In SIRT, however, the correction array is formed with averages over projection angle of the data and guess projections. Additive and multiplicative corrections were considered. Results are shown to be more robust than those obtained with ART, producing smoother solutions. Convergence is initially slower compared with sequential ART. After several (>5) iterations the residuals improve relative to ART solutions.

([25]) sought improvement using a better approximation to the projection process while retaining the fast initial convergence of sequential ART. The Simultaneous Algebraic Reconstruction Technique (SART) calculates the projection sums using bilinear interpolation of the guess array, resulting in smooth corrections. They also use a Hamming window function to smoothly de-emphasize corrections near the edge of the guess array. The results are robust to noise and show a good quality reconstruction after considering each projection angle only once. Although the salt and pepper noise of ART is greatly reduced, it is noted to increase with iteration and is indicative of remaining inconsistency in the projection process combined with sequential correction.

A comparative study of several reconstruction techniques with limited projection data by ([26]) concludes that sequential MART is the overall best algorithm in their tests. ([27]) investigated MART with limited (4-6) projection angles. They proposed the correction be computed as the geometric mean of the corrections due to each projection angle in that pixel. Corrections are applied simultaneously as with SIRT.

They compared the the algorithm to sequential MART algorithms and found it to be more robust, as well as computationally efficient. ([28]) refers to this as simultaneous MART.

The original ART techniques were developed in the context of electron tomography, and the reconstructed quantity was absorption density. ([29]) applied MART to reconstructions where the object was the distribution of intensity as a function of position and wavelength, which seeks simultaneous images and spectra of emitting sources. This is sometimes referred to as snapshot hyperspectral (SHS) imaging.

([30]) proposed that multiple spacecraft views of the optically thin solar corona could be used for three dimensional imaging of coronal structures. They suggested ART as the reconstruction algorithm due to adaptability against nonuniform projection angles and variability in the data due to observation by different spaceraft. They carried out simulations and suggested three to four observation angles were sufficient to obtain useful information about large structures. They also note that due to the back projection nature of the correction that image features are smeared along the lines of sight in the reconstructions, which for small objects look like streaks in the reconstruction. ([31]) used the Smooth Multiplicative Algebraic Reconstruction Technique (SMART) algorithm for simulated three projection coronal tomography. The SMART algorithm is similar to simultaneous MART, but uses adaptive weighting of the corrections to achieve optimal goodness of fit and incorporates a smoothing step in the iteration in an effort to produce smooth solutions in the presence of image noise. Forward projection in that work was done using cubic convolution interpolation, which may represent an improvement over earlier methods (nearest neighbor - ART, and bilinear - SART).

Snapshot hyperspectral imaging of the solar atmosphere was first proposed by ([12]). They described reconstruction of solar transition region spectral line pro-

files via SHS imaging, using multilayer coatings to limit the passband to individual spectral lines. This concept was realized with a successful launch of MOSES, which obtained three angle projection data in the spectral neighborhood of the He II304 Å spectral line. SMART was originally developed for analysis of MOSES data and was applied by ([15]). In addition to choices of smoothing parameters and the control law used for adaptive correction, he further constrained the solution by assuming a fourth projection, the infinite order, based on measured values of average quiet sun spectra near He II304 Å in MOSES passband. Fox reports better results with SMART compared to other methods attempted (iterative Fourier Backprojection and Pixon reconstruction), but notes a tendency of the reconstruction to underestimate doppler shifts in simulations.

In this study, I investigate reconstruction of a MOSES observation of a transition region explosive event (Rust 2017a). The event is a compact brightening on a broad background, whose primary spectral characteristics of blue and red shifted components with 100 km/s line if sight speeds can be inferred directly from the projection data due to the strength of the doppler shifts and the small size of the object. Based on the work of Fox, I used SMART as a starting point. The explosive event reconstruction will be presented in parallel with reconstruction of synthetic data in order to illustrate features of the reconstruction algorithm with a known quantity.

I found that the infinite order correction as implemented over constrains the solution to the point of being unjustifiable. Without this heuristic the reconstruction suffers from streak artifacts. These artifacts take the appearance of continuum emission in reconstructed spectra of compact bright objects. Spectra in the neighborhood of compact objects have the streaked appearance, reminiscent of a plaid pattern, that has been reported by other authors in few projection reconstructions (([30], ([32]). Streak artifacts appear to arise from interaction of compact sources with the broad

background. The broad background is largely indistinguishable between projections, and that part of the image is thus not amenable to reconstruction with the data available; the compact emission is, however. I'll separate the small scale emission of the explosive event from the large scale background emission. Reconstruction of the explosive event on its own removes the streak artifacts and continuum emission, resulting in a much more plausible reconstruction than previously obtained.

I've incorporated the instrument point spread functions in the reconstruction. ([15]) noted how the three MOSES projections appear to have different point spread functions, and showed how this was likely to produce reconstruction artifacts, particularly for small, bright objects. (Rust 2017a) estimated the point spread functions of MOSES images. The point spread functions are incorporated in the reconstructions by combining a ART iteration with a Richardson Lucy (RL) ([21],([22], deconvolution iteration. In that both the reconstruction and the deconvolution are ill posed problems, it seemed best to be even handed between the two, rather than, for example, performing reconstructions on deconvolved data.

All of the above image processing steps - reconstruction, feature extraction, and deconvolution, have the potential to amplify noise in the data. *MOSES* noise has been studied in detail (Rust 2017c). I've used wavelet techniques to incorporate this knowledge into the reconstruction to avoid noise amplification and false structure in the reconstruction. These techniques replace the adaptive weighting and smoothing of SMART, and result in smoother reconstructions.

8.2 Data

The target for reconstruction is the explosive event from chapter 5. Observation date and time is 8 February 2006, 18:47:05 UTC, corresponding to the peak of the light curve of this event.

The data are shown in figure 8.1 and consists of subfields of the *MOSES* $m = -1$, $m = 0$, and $m = +1$ order images, centered on approximately 750"E, 130"S solar heliocentric cartesian coordinates. Subfields are 64×64 pixels, with 0.59" per pixel. The dispersion direction is oriented along the E-W axis, which will correspond to the x axis.

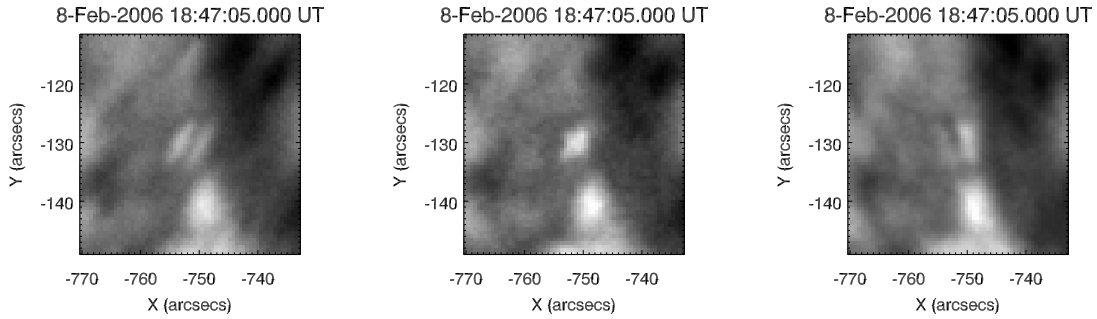


Figure 8.1: An explosive event seen by *MOSES*. Left to right: $m = -1$, $m = 0$, $m = +1$. Panels are 64×64 pixels, with angular sampling 0.59" pixel^{-1}. Dispersion in is 30 km s^{-1} pixel^{-1}. Blue shifted emission moves left (east) in $m = -1$ and right (west) in $m = +1$ relative to $m = 0$.

8.2.1 Synthetic Data

Estimates for the instrument point spread functions (chapter 7) are shown in figure 8.2. I've used these point spread functions to generate synthetic data (figure

8.3) which simulate *MOSES* observations of a compact brightening on a uniform background with the given spectrum. The synthetic data have have additive noise consistent with the observations, and are reconstructed in the same fashion as the real data. The signal to background in the synthetic data were chosen to approximate the real data.

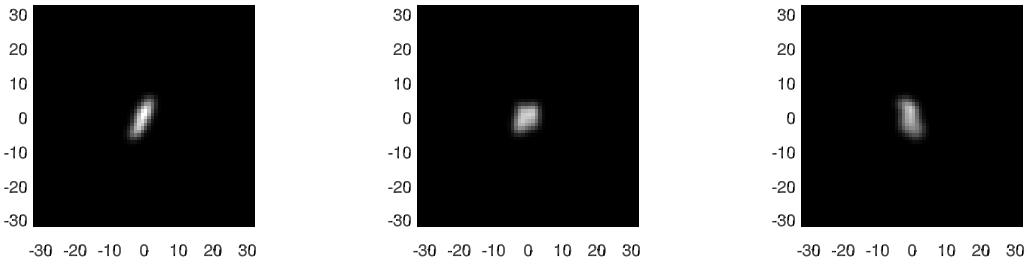


Figure 8.2: *MOSES* point spread function cores in each spectral order, estimated from the data. [RUST PSFS]. Axis units are in pixels, with angular sampling 0.59" pixel^{-1}.

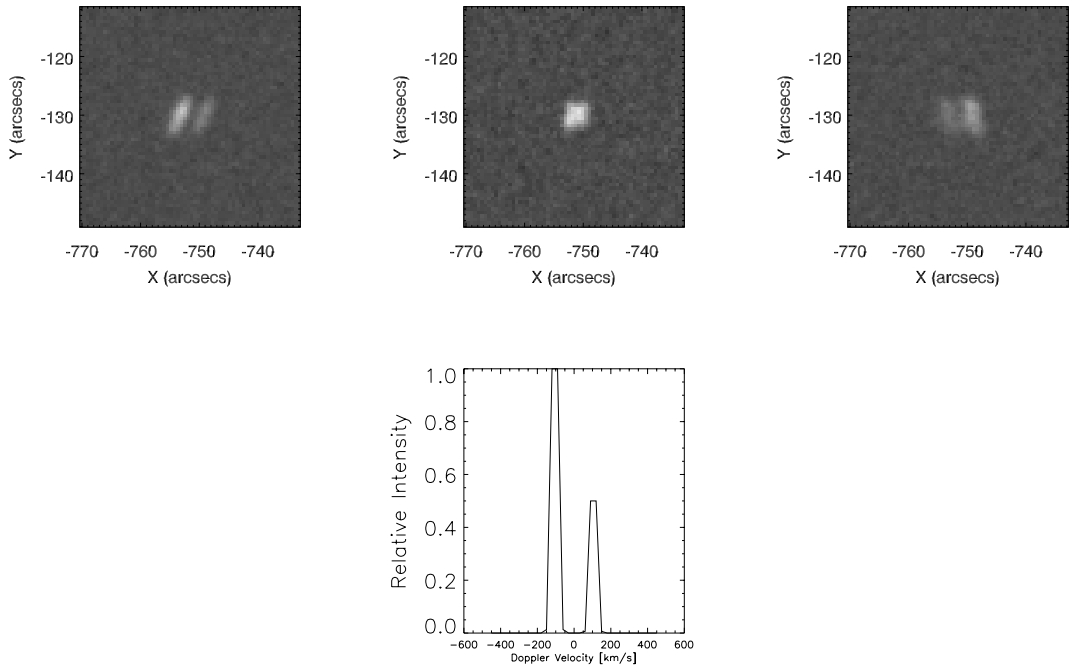


Figure 8.3: Synthetic *MOSES* observation of a small emitting source moving with the plotted velocity profile, set on a uniformly emitting background, assuming the point spread functions of figure 8.2. Left to right: $m = -1$, $m = 0$, $m = +1$. The intensity of the source and background were chosen to approximate those in figure 8.1 (same display scale in both figures). Noise has been added to the synthetic observations consistent with *MOSES* noise model.

8.3 Instrument

MOSES images are formed with a concave spherical diffraction grating. CCDs are located in the focal plane of the $m = -1$, $m = 0$, and $m = -1$ spectral orders. Simultaneous exposure and readout of the three CCDs produces image triplets $\mathcal{I}_m(x, y)$. The distribution of intensity in these images is modeled as

$$\mathcal{I}_m = \{\mathcal{P}_m * \mathcal{I}_m^0\}(x, y) + n(x, y) \tag{8.1}$$

where $\mathcal{P}_m(x, y)$ is the point spread function corresponding to $\mathcal{I}_m$ and $n(x, y)$ is additive noise. $\mathcal{I}_m^0$ is the ideal geometric optics image and is given by ([12], ([15]) as

$$\mathcal{I}_m^0(x, y) = \int_B \nu(x - m\lambda, y, \lambda) d\lambda \tag{8.2}$$

This follows directly from the small angle diffraction equation with dispersion along x. All coordinates are in image pixels, the spatial coordinates are referenced to the center of the mth CCD, and the wavelength is referenced to HeII line center wavelength. B is the instrument passband. The wavelength is related to the pixel width via the dispersion (30 mÅ pixel^{-1}).

Equation 8.2 says that for an ideal instrument, the data are measured projections of the solar spectral irradiance $\nu(x, y, \lambda)$ within the instrument passband. The object is to estimate of ν from $\mathcal{I}_m$. In the units given above, the projection angles correspond to -45, 0 and +45 degrees for $m = -1$, $m = 0$, and $m = 1$ respectively. The instrument passband is dominated by the He II 304 Å spectral line. I assume that the spectral line profile of this explosive event is explained by doppler shifted emission from HeII ions.

8.4 Methods

8.4.1 à trous Discrete Wavelet Transform

The wavelet transform has been applied to many problems in image and signal processing. As the Fourier transform is used to analyze frequency content in periodic data, the wavelet transform is suitable for analysis of data in which features of interest are localized in both position and size. The wavelet transform applied to pixellated data is referred to as the discrete wavelet transform. Many algorithm choices exist when computing the discrete wavelet transform. I've chosen to use the particular algorithm known as the à trous transform.

The à trous transform ([19], [20]) proceeds by application of a low pass filter to an image $\mathcal{I}$ resulting in the smoothed image $\mathcal{I}_s$. The smoothing kernel elements are chosen to be bb^T, where $b = [1, 4, 6, 4, 1]/16$ ([17]).

The difference images $w = \mathcal{I} - \mathcal{I}_s$ are the wavelet coefficients, which represent variability in the image that was lost upon passage from $\mathcal{I}$ to $\mathcal{I}_s$. This lost variability exists in the image within a specific range of spatial size scales. Wavelet coefficients from the à trous transform have mean zero averaged over the image.

Wavelet coefficients representing successively larger image spatial scales are calculated by iterative application, with $\mathcal{I}_s \rightarrow \mathcal{I}$ and halving the filter cutoff frequency at each iteration. Results of the transform up scale N are a set of wavelet coefficient images $w^j, j = 1..N$, where scale increases with j, and the final smoothed image $\mathcal{I}_s^N$. The original image is exactly obtained by $\mathcal{I} = \mathcal{I}_s^N + \sum_j w^j$. $\mathcal{I}_s^N$ and the w^j have the same dimensions as $\mathcal{I}$ (no decimation). A tilde over an image will be used to denote the à trous transform of that image.

8.4.2 Significance Testing

The wavelet coefficients of a noisy image are noisy. When working with noisy images, statistical significance testing can be done on the w^j to differentiate signal from noise. The utility of this resides the fact that noise typically exists at all image scales, whereas an image feature often occupies only a small range of scales. Whether a coefficient is determined to be significant depends on the amplitude of the coefficient relative to possible values given the image noise distribution.

MOSES images show Poisson distributed photon shot noise plus gaussian distributed read out noise [RUST Noise Model]. Signal independent wavelet significance testing of images with this signal dependent noise model is facilitated with the Anscombe transformation ([16], [17]) $\mathcal{I} \rightarrow \hat{\mathcal{I}}$. Similar to square root scaling, with the detector gain accounted for, results in an image whose noise is uniform additive gaussian distributed. The distribution of wavelet coefficients of gaussian noise is gaussian, with standard deviation σ_j at the jth scale.

Significant wavelet coefficients of image $\mathcal{I}$ are determined from $\hat{\mathcal{I}}$. I adopt the hard threshold of $3\sigma_j$. If $|\tilde{\hat{\mathcal{I}}}(x,y,j)| > 3\sigma_j$ then $\tilde{\mathcal{I}}(x,y,j)$ is significant, and assumed to indicate real signal in the data. If $|\tilde{\hat{\mathcal{I}}}(x,y,j)| < 3\sigma_j$ then $\tilde{\mathcal{I}}(x,y,j)$ may have arisen from the noise and is said to be insignificant.

8.4.3 Partial Reconstruction from Significant Wavelet Coefficients

Partial reconstruction from significant wavelet coefficients ([33], [17]) is a means to extract features from an image. It might be thought of as a type of background subtraction. The explosive event is a compact object, which sits on a broad background, which implies the coefficients which describe the object and background are well separated in wavelet space. In this section I present a partial reconstruction of

the explosive event in each order. The technique is the same as was used to estimate the instrument point spread functions from the data [RUST PSF].

An object is generally described by a local maxima among positive, significant coefficients in wavelet space. Significant wavelet coefficients which are connected to the maxima in both scale and space are part of the same object. The object coefficients therefore occupy a volume in wavelet space. The goal of partial reconstruction is to create an image whose wavelet coefficients are the same as those of the object, within the volume on which the object is defined. If the reconstructed image is p, the object coefficients are $\tilde{q}$, and A is the operator which transforms p and projects the result onto the support of $\tilde{q}$, the partial reconstruction problem is minimization of $||Ap-\tilde{q}||$. Solution method is iterative, beginning with $q(x,y) = 0$:

1. Calculate Ap $= \tilde{p}(x,y,j)$
2. Determine the additive error in the coefficients on the support of the object: $\tilde{\epsilon} = \tilde{p} - \tilde{q}$
3. Threshold $\tilde{\epsilon}$; retain only significant coefficients.
4. Calculate correction $\epsilon(x,y) = A^{-1}\tilde{\epsilon}$
5. Update $p = p + \epsilon$
6. Threshold $p > 0$
7. Repeat from steps 1 through 6. Iterations end when no significant coefficients may be found in $\tilde{\epsilon}$

The operator A^{-1} is inverse to the operation A. A projects an image into a list of wavelet coefficients; A^{-1} back projects a list of wavelet coefficients into an image. A^{-1} resolves the stepped appearance created by hard thresholding of the wavelet

coefficients by applying a scale dependent smoothing to the significant coefficients at each scale. The smoothing at scale j, $j > 1$ is implemented by applying the wavelet transform up to scale $j-1$ to the scale j significant coefficients. The result of this transform is $j-1$ wavelet images, and the smooth residual c_{j-1}. The A^{-1} operator replaces the scale j significant residuals with c_{j-1}. I also chose to smooth the scale 1 significant coefficients, with the kernel aa^T, where $a^T = [0.25, 0.5, 0.25]$.

For the example in this paper the scale 2 wavelet coefficients seemed to best represent the objects, and were the only coefficients used in the partial reconstructions. Figure 8.4 shows the scale 2 wavelet coefficients of the observations, and the positive significant coefficients which constitute the object. The results of a reconstruction are shown in figure 8.5.

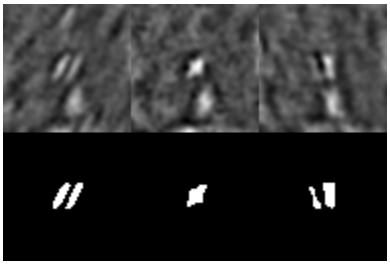


Figure 8.4: Scale 2 wavelet coefficients (top) and the significant coefficients which define the object.

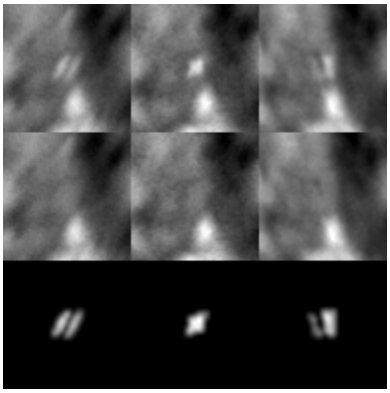


Figure 8.5: Top: Original, Bottom: Explosive event reconstructed from the coefficients in 8.4, and Middle: Residual after reconstruction.

8.4.4 Deconvolution

The deconvolution problem is to determine $\mathcal{I}_m^0$ knowing $\mathcal{I}_m$ and $\mathcal{P}_m$. The difficulty arises in that $\mathcal{P}_m$ has a cutoff frequency, and the noise $n(x, y)$ does not, and efforts to recover high frequency signals can amplify noise. It is highly desirable to avoid introducing spurious image structures during deconvolution, or for that matter at any other step in the reconstruction.

I've chosen to use the Richardson-Lucy (RL) deconvolution algorithm because it conserves flux, results in a positive reconstruction, and the correction step is similar to that from the multiplicative algebraic reconstruction technique (§8.4.5). The basic RL algorithm is

1. Initial guess $g(x, y) = \delta \ll 1$
2. Calculate $g' = g * \mathcal{P}_m(x, y)$
3. Correct: $g = g(\frac{\mathcal{I}_m}{g'} * \mathcal{P}_m(-x, -y))$
4. Iterate

g(x,y) is the estimate for $\mathcal{I}_m$. Noise amplification is minimized by using the the wavelet noise suppression technique described in ([17]). $\mathcal{I}_m$ in step 3 can be written as $\mathcal{I}_m = g'(x,y) + R(x,y)$, where $R(x,y)$ is the residual at a given iteration. R can be thresholded in wavelet space, where coefficients which are not significant are set to zero. For similar reasons as in the partial reconstruction above, the thresholded coefficients are smoothed with the same scale dependent smoothing kernel as is used in partial reconstruction, prior to summing the wavelet coefficients to form the significant residual $\bar{R}$. The algorithm proceeds as above, with the substitution $\mathcal{I}_m \rightarrow (g' + \bar{R})$. Figure 8.6 shows the results of the standard RL deconvolution compared with RL with noise reduction. In the latter the explosive event is significantly sharpened without amplifying the noise structures which give the RL deconvolution a mottled look.

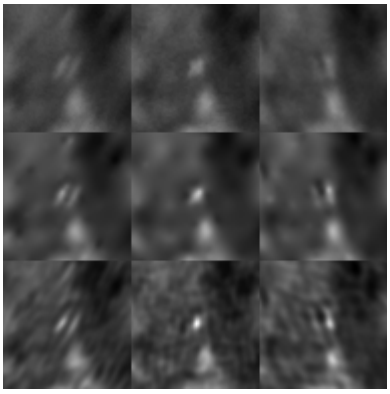


Figure 8.6: Top: Original, Middle: RL deconvolution with wavelet noise supression, and Bottom: Standard RL deconvolution

8.4.5 Algebraic Reconstruction Technique

The goal of algebraic reconstruction is estimation of $\nu(x,y,\lambda)$ from the projections $\mathcal{I}_m$. As noted in the introduction, ART/MART techniques have a long history. The basic MART algorithm is that of ([27]):

1. Initialize guess cube $v(x, y, \lambda) = \delta \ll 1$
2. Project to form guess projections p_m
3. Calculate multiplicative error: $\epsilon_m(x, y) = \mathcal{I}_m / p_m$
4. Extrude $\epsilon_m(x, y)$ along the relevant projection direction to obtain error cubes $\epsilon_m(x, y, \lambda)$
5. Correct: $v = v \prod_m \epsilon_m^{(1/N_m)}$
6. Iterate

The starting point for the reconstructions in this paper was the Smooth Multiplicative Algebraic Reconstruction Technique (SMART), described in ([31] for three view stereoscopic reconstructions. This algorithm smoothes the guess cube prior to the projection in step 2, and uses adaptive weighting in the product in step 5, where the weights are determined based on the χ^2 error statistic. ([15]) used this approach for inversion of MOSES data. In addition to the three measured projections Fox used an inferred projection, which he called the infinite order or $\mathcal{I}_\infty$, corresponding to a projection angle of 90^o, based on average line profile measurements. In addition to these choices, the projection/back-projection steps given the viewing angles of $-45^o, 0^o, 45^o$ are efficiently implemented with array shifting and summing in IDL.

In place of the smoothing and adaptive weighting of SMART I've chosen to use uniform correction weighting and wavelet based noise suppression. This is done in the same fashion as as the RL deconvolution noise suppression, i.e., $\mathcal{I}_m = p_m + \bar{R}$ where again $\bar{R}$ is the significant residual at each step. This results in a smoother reconstruction than that obtained by SMART. I've also abandoned the $\mathcal{I}_\infty$ heuristic used by Fox. This over constrains the solution, resulting in a spectrum in each pixel whose shape is almost identical to the chosen $\mathcal{I}_\infty$.

8.4.6 MART with Deconvolution

Deconvolution is incorporated into MART by enclosing a RL deconvolution iteration inside of the MART iteration. The algorithm is:

1. Initialize guess cube $v(x, y, \lambda) = \delta \ll 1$
2. Project to form guess projections p_m
3. Convolve: $p_m \rightarrow p_m * \mathcal{P}_m(x, y)$
4. Calculate multiplicative error: $\epsilon_m(x, y) = (p_m + \bar{R})/p_m$
5. Convolve: $\epsilon_m \rightarrow \epsilon_m * \mathcal{P}_m(-x, -y)$
6. Extrude $\epsilon_m(x, y)$ along the relevant projection direction to obtain error cubes $\epsilon_m(x, y, \lambda)$
7. Correct: $v = v \prod_m \epsilon_m^{(1/N_m)}$
8. Iterate

8.4.7 MART with Deconvolution and Partial Reconstruction

Incorporating deconvolution into MART results in sharper spectra, but streak artifacts are still present in the reconstructions. This occurs because MART is not able to distinguish between signal in the projections that belongs to different objects. Therefore, object and background signal are allowed to interact, creating streak artifacts. The truth is that the only signal I care about is that of the explosive event; the background is of no interest. Inspired by the partial reconstruction method, I've incorporated these techniques into the MART with deconvolution algorithm. The algorithm is the same as that above, but here $\bar{R}$ takes on a different definition: It is

the residual image produced from the set of wavelet coefficients which are significant *and* belong to the object of interest, i.e., the explosive event.

The results of this type of reconstruction differ slightly from the other reconstructions described. Only the object is reconstructed; the remainder of the projection data is not. Eliminating this remainder, the broad background, is precisely the purpose of this method. For comparison with other methods in §8.5 I chose to reconstruct this remainder separately, using MART with deconvolution, and add it to the results of the object reconstruction.

8.5 Results

I've tested SMART, MART with wavelet noise suppression, MART with deconvolution, and MART with deconvolution and partial reconstruction, on the explosive event observation, as well as the simulated explosive event. For brevity I refer to these as methods 1 through 4, respectively. Methods 2-4 all use wavelet noise suppression. The reconstruction result volume is 64×64 spatial pixels, and 31 wavelength pixels, centered on HeII line center. Methods 1-3 were calculated on domains of 256×256 spatial pixels then cropped to eliminate edge effects. This is not necessary with method 4 as the object is only supported in a small region near the center of the field of view.

The reconstructed projections are shown in figure 8.7 and the residuals are in figure 8.8. The method 3 and method 4 projections are shown after convolution with the point spread functions; the reconstructions are actually much sharper, particularly method 4. Each method is able to fit the observations well enough so the relevant structures in the scene, i.e., the two components of the explosive event, are clear.

The wavelet noise suppression is very effective at removing high frequency noise while retaining image detail. Methods 1 and 2 visually reproduce the observations most closely, particularly method 1 which obliges the noise as well as the signal. Methods 2 and 4 show the best residuals in the sense that coherent structures in the residuals are minimized and the high frequency noise has been filtered out of the reconstruction. These methods (2 and 4) produce very similar residuals, yet the spectra are very different, an inherent difficulty ill posed inverse problems.

Figure 8.9 shows vertical and horizontal slices of the (log scaled) reconstructed irradiance $\nu(x, y, \lambda)$. The horizontal (constant y) slices shows the reconstruction in the dispersion plane. The x axis is horizontal. West increases to the right. In methods 1-3, every peak and valley in the projections produces a streak, as wide, skinny, bright or dark as the peak or valley in question. (x, y, λ) locations where these streaks intersect are amplified. The ratio of the streak amplitude and the amplitude at intersections depends on how many projections intersect. We have a maximum of three, so this ratio is only about 3:1 (see ([32]), fig. 1). In principle, iteration is supposed to improve this ratio in (S)MART. A streak which finds no other intersections should be gradually convinced by the other projections that it does not belong, and is suppressed. However, broad/background emission gives these streaks an excuse to exist, and they are not suppressed in practice. The MART with partial reconstruction algorithm is given additional information about what image features correspond among the projections; in this case the streaks are suppressed. This does not mean that these reconstructions are always accurate; the small bright points emitting at line center reconstructed to the east and west of the synthetic explosive event are artifacts of intersections due only to the extent of the point spread functions. These same artifacts are present in the reconstruction of the real observations as well, but the western bright point probably contains real signal. The method 4

reconstruction resolves a distinct source, emitting near line center, associated with the upper right extension of the object, seen best in figure 8.5. Nevertheless, the method 4 reconstruction is shows fewer artifacts by far then the other methods.

The vertical (constant x) slices shows another way the point spread functions couple into the spectral reconstructions. The y axis is horizontal. In terms of the coordinates in figure 8.1, north points right. The two brighter patches in the center of the panels are the explosive event components, the red component above and the blue component below. As y increases, the reconstructions suggest that the red component gets redder and the blue component gets bluer. This shift is substantial, at least 3 pixels at 30 km/s/pixel. This is similar to the "bipolar jet artifacts" of [15], only in the context of an observation of a true bipolar jet! Incorporating the point spread functions into a standard (S)MART type reconstruction does not solve these problems, and may in fact exacerbate it. Deconvolution in an image context sharpens image features; in this context all features in ν are sharpened, real or not: streaks and intersections due to the point spread functions are sharpened. It is only when partial reconstruction is included that the signal is sharpened and the artifacts are suppressed.

Figure 8.10 shows the reconstructed spectrum averaged over the support (8.4) of the explosive event. In both cases, real and synthetic, the only method able to resolve the shifted components in the explosive event is method 4: MART with deconvolution and partial reconstruction. The method 4 spectrum for the synthetic event shows a bump at zero velocity; this is artifactual as discussed above. It is possible to eliminate this artifact, by applying an algebraic reconstruction directly to the partial reconstruction results (figure 8.5, bottom panel), but caution must be exercised regarding error in the partial reconstruction results. The method 4 reconstruction of the observations shows a significant peak at low velocity. Some of

this appears to be real signal. Looked at carefully, the explosive event has an extension on the upper right, which eventually fades into the background. The method 4 reconstruction resolves two sources, one with low velocity and one with the explosive event profile. It is not known if these sources are physically related.

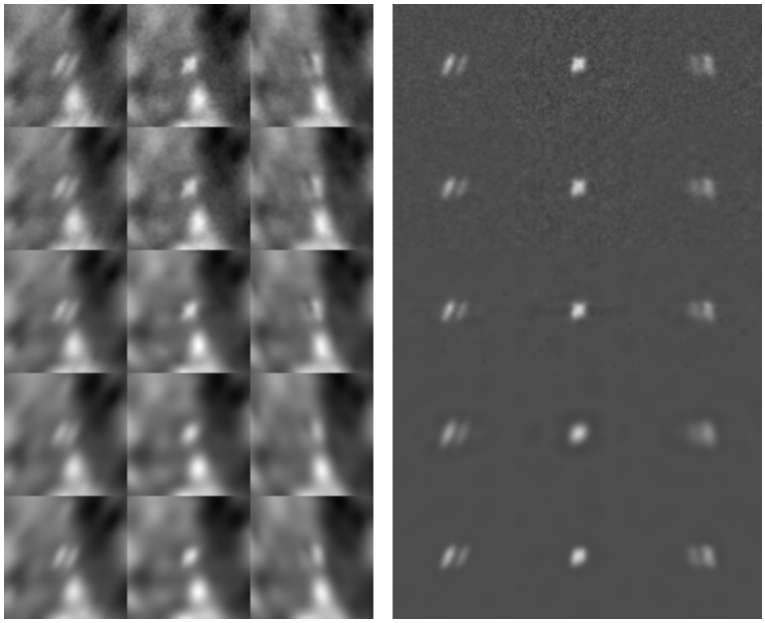


Figure 8.7: Projections, observed (top row) and reconstructed. Left set: real data, Right set: synthetic data. Rows, top to bottom: Observed, Method 1 (SMART), Method 2 (MART with wavelet noise suppression), Method 3(MART with deconvolution), Method 4 (MART with deconvolution and partial reconstruction).

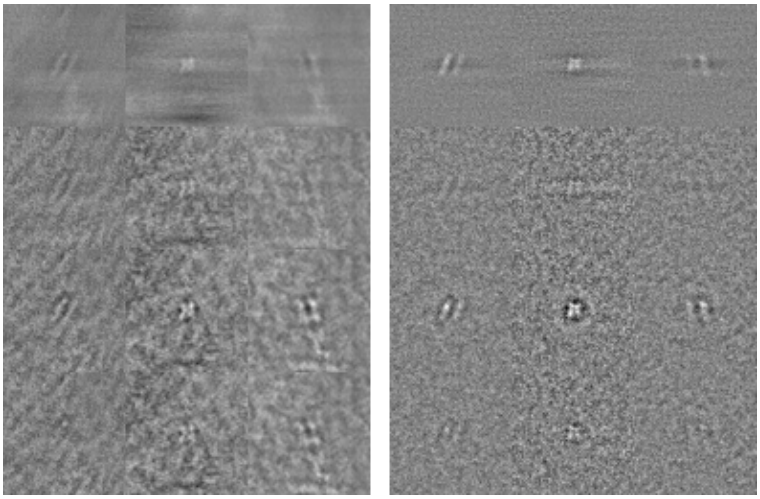


Figure 8.8: Residuals, observed minus reconstructed. Left set: real data; Right set: synthetic data. Rows, top to bottom: Method 1 (SMART), Method 2 (MART with wavelet noise suppression), Method 3(MART with deconvolution), Method 4 (MART with deconvolution and partial reconstruction).

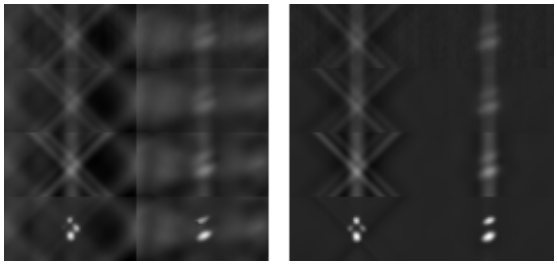


Figure 8.9: Slices through $\log_{10} \nu(x, y, \lambda)$. Left set: real data; Right set: synthetic data. Left column: constant y through explosive event center, x increases to right; Right column: constant x through explosive event center, y increases to right. λ axis is vertical, centered on $\lambda = 0$, increasing upwards. Rows, top to bottom: Method 1 (SMART), Method 2 (MART with wavelet noise suppression), Method 3(MART with deconvolution), Method 4 (MART with deconvolution and partial reconstruction).

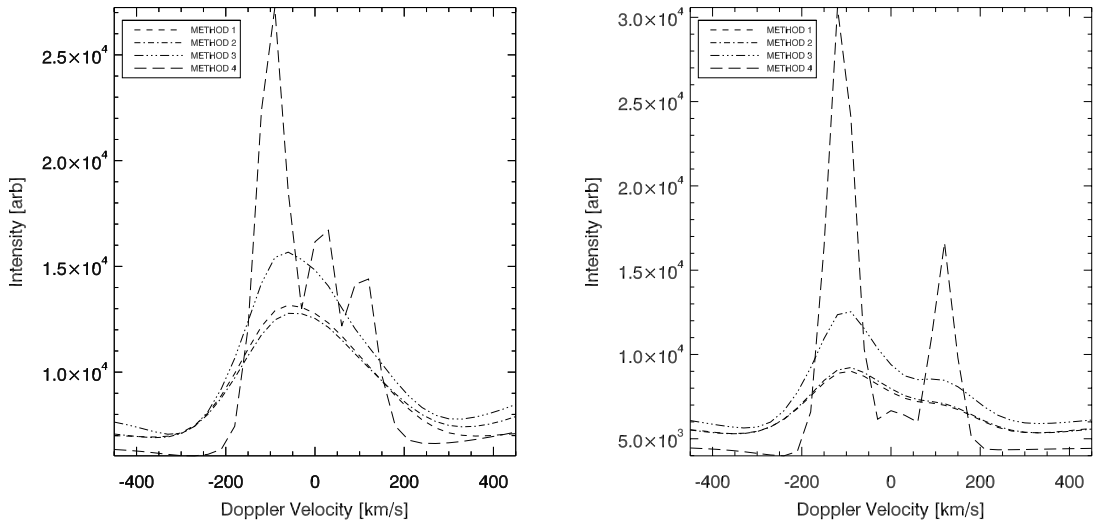


Figure 8.10: Reconstructed average line profile of explosive event. Left plot: real data; Right plot: synthetic data. Method 1 (SMART), Method 2 (MART with wavelet noise suppression), Method 3(MART with deconvolution), Method 4 (MART with deconvolution and partial reconstruction).

8.6 Conclusions

I have investigated algebraic reconstructions of three projection tomography data from the *MOSES* spectrograph. I've incorporated *MOSES* point spread functions and noise model into the reconstructions. While all methods used are able to reproduce the observations, this is not a good indicator of the accuracy of the reconstructions. The data are interpreted as the bi-directional jets of a transition region explosive event. I've also generated and reconstructed a synthetic observation, where the spectrum is known and also represents a bidirectional jet. The only method tested which is

able to reproduce these characteristics is method 4: MART with deconvolution and partial reconstruction.

REFERENCES CITED

[1] E. N. Parker. Nanoflares and the solar X-ray corona. *ApJ*, 330:474–479, July 1988. doi:10.1086/166485.

[2] K. P. Dere, J.-D. F. Bartoe, G. E. Brueckner. Explosive events in the solar transition zone. *SoPh*, 123:41–68, March 1989. doi:10.1007/BF00150011.

[3] K. P. Dere, J.-D. F. Bartoe, G. E. Brueckner, J. Ewing, P. Lund. Explosive events and magnetic reconnection in the solar atmosphere. *J. Geophys. Res.*, 96:9399–9407, June 1991. doi:10.1029/90JA02572.

[4] C. C. Kankelborg, A. B. C. Walker, II, R. B. Hoover, T. W. Barbee, Jr. Observation and Modeling of Soft X-Ray Bright Points. I. Initial Results. *ApJ*, 466:529, July 1996. doi:10.1086/177529.

[5] D. E. Innes, B. Inhester, W. I. Axford, K. Wilhelm. Bi-directional plasma jets produced by magnetic reconnection on the Sun. *Nature*, 386:811–813, April/n 1997. doi:10.1038/386811a0.

[6] W. Curdt, H. Tian. Spectroscopic evidence for helicity in explosive events. *A&A*, 532:L9, August/n 2011. arXiv:1107.1969, doi:10.1051/0004-6361/201117116.

[7] D. E. Innes. Coordinated observations of the quiet Sun transition region using SUMER spectra, TRACE images and MDI magnetograms. *A&A*, 378:1067–1077, November 2001. doi:10.1051/0004-6361:20011177.

[8] A. R. Winebarger, A. C. Updike, K. K. Reeves. Correlating Transition Region Explosive Events with Extreme-Ultraviolet Brightenings. *ApJL*, 570:L105–L108, May 2002. doi:10.1086/341121.

[9] D. E. Innes, L. Teriaca. Quiet Sun Explosive Events: Jets, Splashes, and Eruptions. *SoPh*, 282:453–469, February 2013. arXiv:1210.7667, doi:10.1007/s11207-012-0199-y.

[10] Z. Huang, M. S. Madjarska, L. Xia, J. G. Doyle, K. Galsgaard, H. Fu. Explosive Events on a Subarcsecond Scale in IRIS Observations: A Case Study. *ApJ*, 797:88, December 2014. arXiv:1409.6425, doi:10.1088/0004-637X/797/2/88.

[11] J. L. Fox, C. C. Kankelborg, R. J. Thomas. A Transition Region Explosive Event Observed in He II with the MOSES Sounding Rocket. *ApJ*, 719:1132–1143, August/n 2010. doi:10.1088/0004-637X/719/2/1132.

[12] Charles C. Kankelborg, Roger J. Thomas. Simultaneous imaging and spectroscopy of the solar atmosphere: advantages and challenges of a 3-order slitless spectrograph, 2001. doi:10.1117/12.450074.

[13] D. E. Innes, L.-J. Guo, Y.-M. Huang, A. Bhattacharjee. IRIS Si IV Line Profiles: An Indication for the Plasmoid Instability during Small-scale Magnetic Reconnection on the Sun. *ApJ*, 813:86, November 2015. arXiv:1509.08837, doi:10.1088/0004-637X/813/2/86.

[14] J.R. Janesick. *Scientific Charge-coupled Devices*. Press Monograph Series. Society of Photo Optical, 2001.

[15] James Lewis Fox. *Snapshot imaging spectroscopy of the solar transition region: The Multi-Order Solar EUV Spectrograph (MOSES) sounding rocket mission*. Doctoral Dissertation, Citeseer, 2011.

[16] F. J. ANSCOMBE. The transformation of poisson, binomial and negative-binomial data. *Biometrika*, 35(3-4):246, 1948. arXiv:/oup/backfile/Content_public/Journal/biomet/35/3-4/10.1093/biomet/35.3-4.246/2/35-3-4-246.pdf, doi:10.1093/biomet/35.3-4.246.

[17] J.-L. Starck, F. Murtagh, A. Bijaoui. *Image Processing and Data Analysis: The Multiscale Approach*. Cambridge University Press, New York, NY, USA, 1998.

[18] R. A. Harrison. EUV Blinkers: The Significance of Variations in the Extreme Ultraviolet Quiet Sun. *SoPh*, 175:467–485, October 1997. doi:10.1023/A:1004964707047.

[19] Matthias Holschneider, Richard Kronland-Martinet, Jean Morlet, Ph Tchamitchian. A real-time algorithm for signal analysis with the help of the wavelet transform. *Wavelets*, pages 286–297. Springer Berlin Heidelberg, 1990.

[20] Mark J Shensa. The discrete wavelet transform: wedding the a trous and mallat algorithms. *IEEE Transactions on signal processing*, 40(10):2464–2482, 1992.

[21] William Hadley Richardson. Bayesian-based iterative method of image restoration*. *J. Opt. Soc. Am.*, 62(1):55–59, Jan 1972. doi:10.1364/JOSA.62.000055.

[22] L. B. Lucy. An iterative technique for the rectification of observed distributions. *AJ*, 79:745, June 1974. doi:10.1086/111605.

[23] Richard Gordon, Robert Bender, Gabor T Herman. Algebraic reconstruction techniques (art) for three-dimensional electron microscopy and x-ray photography. *Journal of theoretical Biology*, 29(3):471IN1477–476IN2481, 1970.

[24] Peter Gilbert. Iterative methods for the three-dimensional reconstruction of an object from projections. *Journal of theoretical biology*, 36(1):105–117, 1972.

[25] Anders H Andersen, Avinash C Kak. Simultaneous algebraic reconstruction technique (sart): a superior implementation of the art algorithm. *Ultrasonic imaging*, 6(1):81–94, 1984.

[26] Dean Verhoeven. Limited-data computed tomography algorithms for the physical sciences. *Applied optics*, 32(20):3736–3754, 1993.

[27] D. Mishra, K. Muralidhar, P. Munshi. a Robust Mart Algorithm for Tomographic Applications. *Numerical Heat Transfer Part B - Fundamentals*, 35:485–506, June 1999. doi:10.1080/104077999275857.

[28] C. Atkinson, J. Soria. An efficient simultaneous reconstruction technique for tomographic particle image velocimetry. *Experiments in Fluids*, 47:553–568, October 2009. doi:10.1007/s00348-009-0728-0.

[29] Takayuki Okamoto, Ichirou Yamaguchi. Simultaneous acquisition of spectral image information. *Opt. Lett.*, 16(16):1277–1279, Aug 1991. doi:10.1364/OL.16.001277.

[30] J. M. Davila. Solar Tomography. *ApJ*, 423:871, March 1994. doi:10.1086/173864.

[31] C. C. Kankelborg. Coronal Tomography. *ArXiv e-prints*, June 2008. arXiv:0806.4803.

[32] MI Agafonov. Few-projection tomography. i. radio-astronomical approach for the problem and the 2-clean dsa method. *Radiophysics and quantum electronics*, 47(2):85–99, 2004.

[33] Albert Bijaoui, Frédéric Rué. A multiscale vision model adapted to the astronomical images. *Signal processing*, 46(3):345–362, 1995.

APPENDICES

Appendix Figs Here Appendix Code Here